Protein Turbines I: The Bacterial Flagellar Motor

Timothy C. Elston* and George Oster#
*Center for Nonlinear Studies and Theoretical Division, Los Alamos National Laboratory, Los Alamos, New Mexico 87545, and
#Department of Molecular and Cellular Biology, University of California, Berkeley, California 94720-3112 USA

ABSTRACT The bacterial flagellar motor is driven by a flux of ions between the cytoplasm and the periplasmic lumen. Here we show how an electrostatic mechanism can convert this ion flux into a rotary torque. We demonstrate that, with reasonable parameters, the model can reproduce many of the experimental measurements.

INTRODUCTION

The bacterial flagellar motor (BFM) is a rotary engine that derives its energy from the electrochemical gradient established between the cell cytoplasm and the periplasmic lumen. This gradient drives ion flow through the motor, which is transduced into a rotary torque. When the motor rotates counterclockwise, the helical flagella propagate a wave away from the cell body. This causes adjacent flagella to intertwine and form a propulsive corkscrew that drives the bacterium through the fluid medium at speeds of up to 25 μm/s (Anderson, 1975; Childress, 1981). When the motors reverse their direction of rotation, the individual flagella fly apart, causing the bacterium to tumble (Macnab, 1977). When the flagella reverse again to their swimming mode, the bacterium's direction has been randomly reoriented. Normally, reversals occur spontaneously around 1/s. However, a bacterium can bias its random walk up concentration gradients of chemoattractants by adjusting its tumbling frequency (Berg, 1983).

Many models have been proposed for this molecular engine (reviewed by Laüger, 1990). Here we propose a novel mechanism for transducing an electrochemical potential gradient into a mechanical torque, compare its performance with experimental observations, and contrast it with earlier models.

PROPERTIES OF THE BACTERIAL FLAGELLAR MOTOR

Although a complete molecular structure of the flagellar motor is not yet available, microscopic, biochemical, and genetic studies have sketched a rough geometrical picture of motor assembly (Katayama et al., 1996; Macnab, 1996; Schuster and Khan, 1994; Sharp et al., 1995a). Fig. 1 is a schematic diagram showing the major components and their relative sizes (Francis et al., 1994; Schuster and Khan, 1994). The energy-transducing elements consist of the C-ring, believed to constitute the rotor, and the 8–16 MotA/MotB complexes, believed to constitute the torque-generating stator elements. The rotor radius is ~20–25 nm and probably carries charges around its periphery (Macnab, 1996). The MotA and MotB proteins consist of four and one transmembrane α-helices, respectively, and are thought to be proton channels. The site of torque generation appears to be the cytoplasmic domain of MotA, which also contains α-helical domains (Sharp et al., 1995a, b; Tang et al., 1996).

The motor is driven by the electrochemical potential gradient between the intermembrane space and the cytoplasm. In most bacteria (e.g., *Escherichia coli*) this gradient is set up by proton pumps; however, protonation may not play an essential role in the transduction, because other flagellar motors are driven by sodium. At low speeds, the motor torque appears to be roughly proportional to the "proton-motive force," defined as PMF $\equiv \Delta\psi - (2.3\ RT/F)\Delta$pH, where F is the Faraday constant, R the gas constant, T the absolute temperature, ΔpH the pH difference between the lumen and cytoplasm, and $\Delta\psi$ the transmembrane potential (50–200 mV). In terms of motor performance, a ΔpH of 2 is roughly equivalent to a membrane potential difference of 120 mV. Kinetic studies suggest that, at normal swimming conditions of ~100 Hz, ~1200 protons pass through the motor per revolution, or ~10^5 protons/s.

A variety of techniques have been applied to determine the mechanical behavior of the motor (Berg, 1995; Berg and Turner, 1993; Berry and Berg, 1996; Meister and Berg, 1987). These experiments have measured the rotor speed as a function of an externally applied torque. From the load-velocity curve, the motor torque versus velocity curve can be directly computed. Fig. 2 describes the major features of these relationships. In the absence of an external torque, a tethered bacterium rotates at $\omega_0 \approx 10$ Hz. The rotational drag coefficient is $\zeta \approx$ 5–10 pN-s-nm. (The rotational drag coefficient of a cylinder of length L and radius r spinning about its base in a fluid of viscosity η is $\zeta = 4\pi\eta Lr^2$. For a bacterium 3 μm long with a 0.5-μm radius in water, $\zeta \approx$ 5–10 pN-nm-s.) Thus the torque developed by the motor is ~300–600 pN-nm. For 10 stator elements, each stator develops ~30–60 pN-nm, and the motor speed increases linearly with the number of active stators.

In addition to measuring the mean velocity as a function of load, important information can be gleaned from studies

Received for publication 5 February 1997 and in final form 28 April 1997.
Address reprint requests to Dr. George Oster, Department of ESPN, University of California, 201 Wellman Hall, Berkeley, CA 94720-3112. Tel.: 510-642-5277; Fax: 510-642-5277; E-mail: goster@nature.berkeley.edu.

0006-3495/97/08/703/19 $2.00

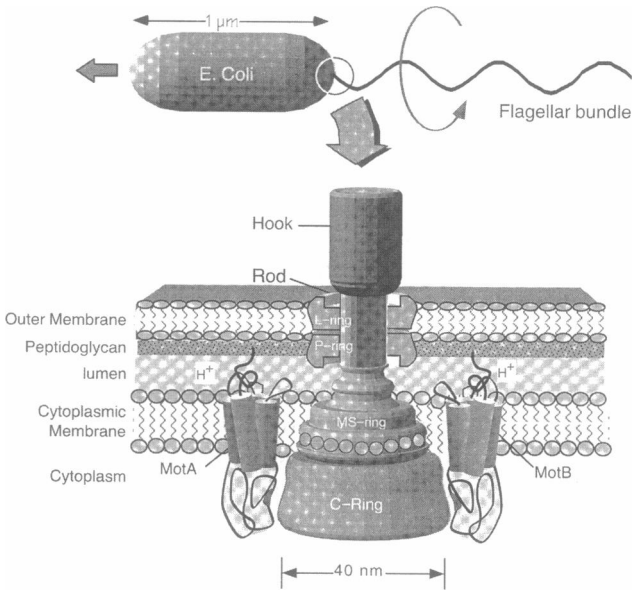

FIGURE 1 Motor structure. The flagellar rod passes through a series of rings. The L (lipid) ring, P (peptidoglycan) ring, and MS (membrane-supramembrane) rings are thought to act as structural bushings, anchoring the motor to the cell wall. The C (cytoplasmic) ring is thought to be the motor rotor, and consists of the three proteins FliG, FliM, and FliN. The stator elements consist of 8–16 MotA/MotB complexes. Each MotA consists of four α-helices that have a large cytoplasmic domain. Each MotB is a single α-helix that is anchored to the peptidoglycan layer. Together, the five α-helices of the MotA/MotB complex constitute a channel that conducts protons from the lumen to the cytoplasm.

on the statistical variability of the motor's motion under different circumstances. In particular, first-passage time statistics (e.g., time to rotate a given number of revolutions) at low speeds suggest that the motor operates nearly like a "stepper"; that is, a fixed step size is taken at random times (Samuel and Berg, 1995). Like other statistical measures, these experiments provide information that is independent of mean value measurements and can be used to make independent estimates of motor characteristics (Peskin and Oster, 1995; Svoboda et al., 1994).

THE ION TURBINE: FIXED STATOR MODEL

The operating principle of the ion turbine is quite simple, and can be understood as follows. Consider two cylindrical surfaces in close apposition, and constrained so that their only degree of freedom is for the inner cylinder to rotate with respect to the fixed outer cylinder. On each surface place an arbitrary distribution of point charges. In general, the electrostatic potential field defined by the charge distributions will have many equilibria, and in the absence of any constraints the inner surface will rotate by some angle until mechanical equilibrium is achieved in some local minimum. Suppose a single positive ion is now placed on one of the negative charges, thus neutralizing it. Then the system will no longer be in mechanical equilibrium and the inner cylinder will rotate to a new local equilibrium position. To turn this system into a rotary motor, the fixed charges must be located in such a way that the successive equilibria cause the cylinders to rotate in one direction. There is no unique solution to this geometrical problem; however, we shall construct one plausible charge geometry based on certain structural features of the *E. coli* flagellar motor.

In the bacterial flagellar motor, the proton path is somewhat ambiguous. It is generally thought to follow the α-helices of the MotA/MotB channel complex. But the torque-generating regions appear to be the cytoplasmic domain of MotA, which abuts the FliG component of the rotor. Blair and co-workers have isolated acidic and basic residues on both rotor (FliG) and stator (MotA and MotB) that appear to be necessary for torque generation (Lloyd and Blair, 1997; Tang et al., 1996). Here we will illustrate the principle of torque generation by separating the acidic residues that constitute the protonation sites and the basic residues that constitute the gating sites on the stator and rotor, respectively. Fig. 3 shows a schematic of the model.

We will assume that the rotor carries positive charges arranged in helical rows. Each row consists of four charges spaced in a 2 + 2 configuration, shown in Fig. 3. Each of the eight stators carries two negative charges located vertically between the two positive rotor charges. We emphasize that many charge configurations are possible, and it is not necessary to segregate positive charges on the rotor and negative charges on the stator, although there is some experimental support for this choice. What is necessary is the tilt of the rotor charges with respect to the stator charges, although it is equally effective to have the rotor charges vertical and the stator charges tilted. We have chosen the simple charge distribution shown in Fig. 3 for illustrative purposes, and we shall speak of the mobile ions as protons, but the same argument applies to the sodium-driven motor. Initially, we will assume that the stator is rigid and immovable; later we shall relax this assumption.

When a positive rotor charge is not blocking their entrance, protons can enter the stator from the top (periplasmic space) to associate with the top negative charge on the stator. When the middle rotor charges are not blocking the proton's path, it can jump to the lower stator charge, and when the bottom charge rotates out of the way, the proton can hop out to the cytoplasm. The ability of the proton to proceed through the stator depends on the rotor's angular position, θ, for this determines the electrostatic landscape the proton must traverse. This landscape is specified by the charge distribution on the rotor and on the stator. Denote by $V(\theta, z)$ the electrostatic potential field set up by the distribution of fixed charges on the rotor and stator. Fig. 5 *a* shows the electrostatic surface experienced by a proton as it passes through the stator. (In computing the electrostatic field, we have neglected the rotor curvature.)

The force exerted on the rotor by a stator depends on the occupancy of the stator charged sites. We will model the stator sites as Coulomb potential wells, the depth of which we estimate from the pK_a of glutamic and aspartic acid residues that could comprise the stator sites. The potential

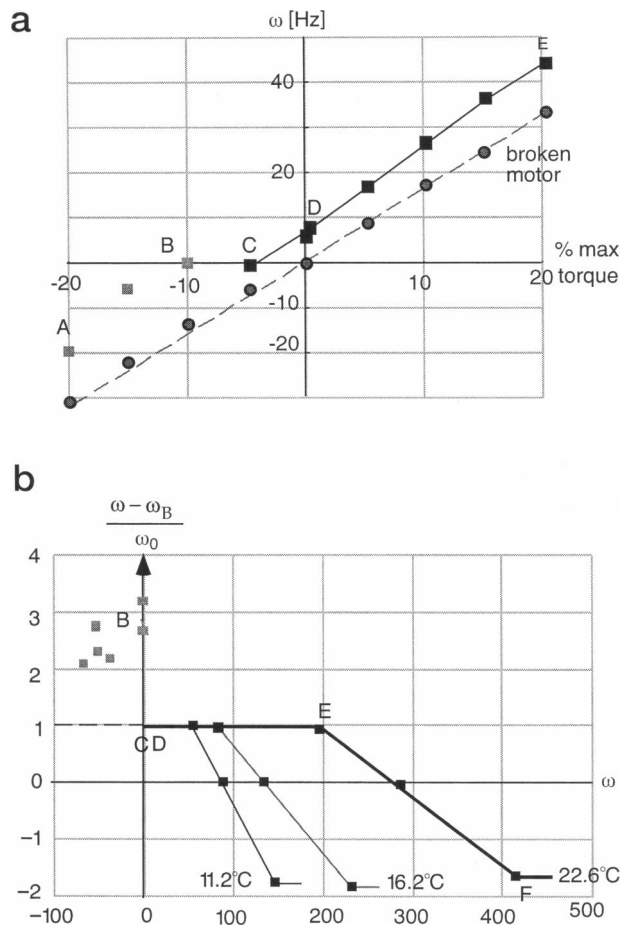

FIGURE 2 Mechanical behavior of the *E. coli* bacterial flagellar motor. Using an electrorotation method on tethered bacteria, Berg and Turner were able to measure the intrinsic motor torque as a function of rotor speed (Berg and Turner, 1993). (*a*) Plot of the rotor angular velocity, ω, for an active motor versus the percentage of the maximum torque applied by the electrorotation apparatus. □, Data for a functioning motor; ○, data for a broken motor with no internal torque generation; ····, least-squares fit to the broken motor data (data taken from Berg and Turner, 1993, their figure 10). Here torque is taken as positive in the direction of the motor's intrinsic motion (counterclockwise for the mutants employed by Berg and Turner), so that positive torque corresponds to driving the rotor forward, and negative torque opposes the rotor's motion. There are four regimes. The zero load velocity, $\omega(\tau = 0) = \omega_0$, is located at *D* in *a*. Between *D* and *C* the motor speed decreases linearly as the torque opposing the motor increases. At the stall torque, *C*, an apparent barrier to reverse rotation is encountered that persists until point *B*, whereupon the motor velocity once again decreases linearly as it is driven in reverse, until it breaks at point *A* (motors generally break when driven too hard in reverse). The region of the torque-velocity curve between *A* and *C* is due largely to nonlinearities in the electrorotation apparatus (Berry and Berg, 1996), and so those data are indicated by gray squares. The torque-velocity curve for a broken motor is practically linear, passing through the origin. Above point *E* the motor velocity rises less steeply with torque; eventually it crosses the broken motor curve, indicating that the motor is adding more drag to the electrorotation apparatus than a broken motor (not shown in this data set). Subtracting the broken motor curve from the working motor compensates for the frictional dissipation at each velocity, and gives the internal torque developed by the motor. This is shown in *b*, where the normalized motor torque, $(\omega - \omega_{broken})/\omega_0$, is plotted versus the rotor speed for three different temperatures. Data points corresponding to the apparent barrier to reverse rotation in *a* arising from the apparatus are also gray. The key features of this graph are the constant-torque plateau below ~100 Hz and the sharp break and linear decrease until saturation, because at high enough driving torque the contribution of the motor becomes negligible. The linear decrease in motor torque occurs when the driving torque is spinning the motor faster than its internal mechanism would drive it.

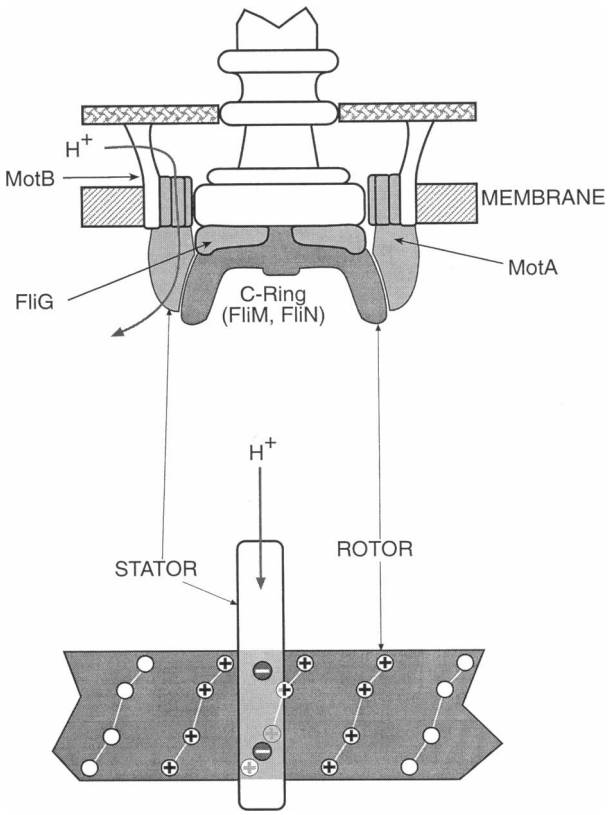

FIGURE 3 (*Top*) Schematic of the rotor and stator configuration. Protons flow downward from the periplasmic space, through the MotA/MotB channel complex, and into the cytoplasmic domain of MotA, where they are subject to the composite electrostatic field of the rotor (FliG) and stator (MotA/B) charges. In the model we assume that protons flow exclusively through the stator. (*Bottom*) The charge distribution used in our simulations. In this configuration the stator charges are negative (●) and the rotor charges are positive (○). The rotor is divided into $n = 15$ repeating units consisting of four charges spaced in a 2 + 2 configuration, giving a total of 60 positive rotor charges. The length of each unit is $2\pi R/n$, and the horizontal spacing between charges is $\pi R/2n$. If L (= 8 nm) is the height of the rotor, then the vertical position of the four charges is given by (0, $L/4$, $3L/4$, L). The charges on the stator are located at ($L/8$, $7L/8$). The gap separating the rotor and stator is 0.7 nm. The closest approach of the protons to the stator charges is 0.5 nm.

seen by the proton is the composite of the field set up by the rotor and stator charges. We model the transition rates between stator states by the Kramers rate theory (Hanggi et al., 1990). This assumes that the protons are in thermal equilibrium in each potential well, and that the time the proton spends in transit between sites is much shorter than the time spent in each potential well (this assumption is justified in Appendix A). For a stator with two negatively charged sites, there are four possible stator states corre-

sponding to the four possible proton occupancies:

$\begin{pmatrix}\circ\\ \circ\end{pmatrix}$ = E: both sites empty

$\begin{pmatrix}\bullet\\ \circ\end{pmatrix}$ = T: top site occupied

$\begin{pmatrix}\circ\\ \bullet\end{pmatrix}$ = B: bottom site occupied

$\begin{pmatrix}\bullet\\ \bullet\end{pmatrix}$ = F: both sites full

Thus we describe the state of each stator by the Markov chain shown in Fig. 4. Denote by $\mathbf{p}(t)$ the state vector of the stator, i.e., the probabilities of finding the stator in each of the states (E, T, B, F) at time t. The dynamics of the Markov chain is described by the evolution of the state vector:

$$\frac{d\mathbf{p}}{dt} = \mathbf{K}(\theta)\cdot\mathbf{p} \tag{1}$$

where the transition matrix, $\mathbf{K}(\theta)$, can be read from the transition diagram in Fig. 4:

$$\mathbf{K} = \begin{pmatrix} -(k_{ET}+k_{EB}) & k_{BE} & 0 \\ k_{ET} & -(k_{TE}+k_{TB}+k_{TF}) & k_{BT} \\ k_{EB} & k_{TB} & -(k_{BE}+k_{BT}+k_{BF}) \\ 0 & k_{TF} & k_{BF} \end{pmatrix} \quad \begin{matrix} k_{FT} \\ k_{FB} \\ -(k_{FT}+k_{FB}) \end{matrix} \tag{2}$$

The transition operator, $\mathbf{K}(\theta)$, depends on the angular position of the rotor, because the ability of an ion to jump between stator sites depends on the electrostatic potential field at each rotor angle, θ. The transition rates are computed from a modification of the Kramers formula (Hanggi et al., 1990):

$$k_{ij} \propto \frac{D_p}{\Delta z^2} e^{-\Delta V_{ij}/k_B T}, \qquad i,j = \text{E, T, B, F} \tag{3}$$

where D_p is the proton diffusion coefficient, Δz is half the distance between sites, and V_{ij} are the electrostatic potential heights separating the different sites. For transitions into and out of the stator, Eq. 3 must be modified to account for the lumenal or cytoplasmic proton concentration (see Appendix A).

The motion of the rotor is described by equating the force exerted on the rotor by the stators to the viscous drag exerted by the surrounding fluid. This yields the following Langevin equation for the rotor angular velocity $\omega = d\theta/dt$:

$$\underbrace{\zeta_R \frac{d\theta}{dt}}_{\substack{\text{Viscous}\\ \text{drag}}} = \underbrace{\tau_M(\theta,t)}_{\substack{\text{Motor}\\ \text{Load}}} - \underbrace{\tau_A}_{\substack{\text{Load torque}\\ \text{applied to}\\ \text{the rotor}}} + \underbrace{f_R(t)}_{\substack{\text{Brownian}\\ \text{force}}} \tag{4}$$

where the motor torque is generated by the electrostatic interaction between the rotor and stator:

$$\tau_M(\theta,t) = \underbrace{\sum_{i=1}^{N} -\frac{\partial V_i^j(\theta,t)}{\partial\theta}}_{\substack{\text{Electrostatic force applied}\\ \text{by } N \text{ stators}\\ \text{to the rotor}}}, \qquad j \in \{\text{E, T, B, F}\} \tag{5}$$

Here ζ_R is the viscous drag of the motor assembly corresponding to a flagellum or to an entire cell. τ_A is the load torque applied to the motor by the experimental apparatus, and $f_R(t)$ is the Brownian force on the rotor. We model the Brownian force in the usual way, as uncorrelated Gaussian noise: $\langle f(t)\cdot f(s)\rangle = \sqrt{2k_B T\zeta_R}\,\delta(t-s)$ (Doering, 1990). The potential, $V_i^j(\theta,t)$, driving the rotor depends on the angular position of the rotor, θ, and which state each of the N stators happens to be in. Because we have discretized the proton's vertical position in the stator, there are four possible potentials on the right-hand side of Eq. 4 corresponding to the four possible configurations of the proton in the stator [E, T, B, F]. Each potential is computed from Coulomb's law from the distribution of rotor and stator charges as described in Appendix A. For simplicity, we shall assume that the charges of the stator sites are -1, so that a proton occupying a site completely neutralizes it. Therefore, in the F (Full) state, where both stator sites are occupied, $V_F = 0$.

Equations 1 and 4 constitute a stochastic description of the motor. This is a doubly stochastic process: $f_R(t)$ describes the Brownian fluctuations of the rotor, and $T(\theta)$ describes the Markov transitions of the proton between the four states of the stator. In Appendix D we describe the numerical method for simulating these equations. (*Note*: The trajectories of Eqs. 1 and 4 yield sample paths for the doubly stochastic process governing the rotor motion. To obtain good statistics about the motor's behavior, one must

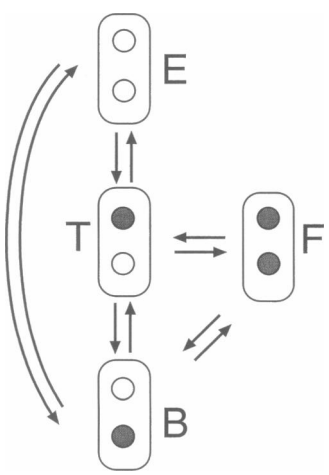

FIGURE 4 The Markov chain describing the four possible stator states corresponding to a stator with two negatively charged ion-binding sites. The transition rates between the states $k_{ij}(\theta)$ depend on the rotor position, θ, which determines the potential field experienced by the mobile ion, $V_i(\theta, z)$, i = E, T, B, F.

average over many realizations—or one long realization—of the process. An equivalent way of representing the system is to describe the rotor motion by the Fokker-Planck equations:

$$\frac{\partial \mathbf{P}}{\partial t} = [\mathbf{L}(\theta) + \mathbf{K}(\theta)] \cdot \mathbf{P} \tag{6}$$

where $\mathbf{P}(\theta, t)$ is the probability distribution vector for the rotor being at angular position θ at time t. $\mathbf{L}(\theta)$ is a diffusion operator and $\mathbf{K}(\theta)$ is the transition matrix given in Eq. 2. This approach is described in more detail in Appendix A; it yields the entire probability distribution for the rotor's position, albeit at the price of a much more formidable numerical computation.)

The operation of the motor can be understood intuitively by following the path of a point on the rotor as a proton progresses through the potential field set up by the rotor and stator charges. In Fig. 5 *b* we have plotted the three nonzero potentials, $V_i(\theta)$, corresponding to the stator states. The trajectory of the rotor in each state is always down the potential gradient toward a local minimum; however, when it reaches the minimum in one state, a thermal fluctuation can cause it to jump to another state and continue in that state down the new potential. If the sequence of potentials is monotonic in θ, then the rotor will always turn in that direction. The pattern of the proton movements is determined by the placement of charges. The charge geometry we have selected is only illustrative; the true charge arrangement must be gleaned from structural information about the distribution of charged amino acids on the rotor and on the MotA/MotB channel helices.

Note that the tilted geometry of the rotor and stator charge distributions confers upon the assembly the property of a "gated" ion channel: protons are more likely to enter only in certain angle intervals when the upper blocking charge is not occluding the channel entrance. Once in the upper stator site, the proton is more likely to jump to the bottom stator site if the rotor moves forward, and it can more easily exit from the lower site when the rotor moves forward again to remove the blocking charge at the exit (cf. Fig. 5 *b*). This progression of "gates" controls the ion flux through a stator element and couples it to the rotation rate of the rotor.

The energy transduction between the electrochemical potential gradient across the membrane and the motor torque is indirect. The hopping of the protons between the stator charge sites is driven by thermal energy. When a hop takes place, the electrostatic potential field shifts and exerts a torque on the rotor. The geometry of the rotor charges gates the protons sequentially through the stator, and the electrochemical potential biases this sequence downward. The magnitude of the electrostatic torque is limited by the thermal energy required to hop out of a potential well; thus the electrochemical potential difference is transduced by the proton's biased diffusion into an electrostatic torque. In Fig. 5 *b* each proton hop out of the $\sim 10 k_B T$ stator well yields $\sim 5 k_B T$ of work performed on the rotor. This is because we have placed the rotor and stator charges 0.7 nm away from each other, which attenuates the electrostatic coupling between them; if we were to narrow this gap, or to reduce the dielectric constant of the stator, the transduction would be more efficient.

Two approximations

In the following section we will present numerical simulations of the model Eqs. 1–4. However, there are two approximations that, under certain circumstances, render the computations easier to perform.

Smooth running

It is tempting to assume that the motor runs smoothly, $\theta = \omega t$, so that one can compute the mean motor torque, $\langle \tau_M \rangle$, by averaging Eq. 4 over a cycle:

$$\langle \tau_M \rangle \approx \frac{1}{T} \sum_{i=1}^{4} \int_0^{\tau} p_i(\omega t) \tau_M(\omega t) \mathrm{d}t \tag{7}$$

where the instantaneous motor torque, $\tau_M(\theta(t))$, is calculated from the electrostatic potential, Eq. 5, and T is the time required for the rotor to move through one period. Then the angular velocity is related to the motor and applied torques simply by

$$\zeta_R \langle \omega \rangle = \langle \tau_M \rangle + \langle \tau_A \rangle \tag{8}$$

However, the assumption that the motor runs smoothly contradicts the experiments which indicate that the motor is a "stepper" (Samuel and Berg, 1996). However, Eq. 7 is probably a good approximation when many stators are operating or when the motor is driven by a high external torque. This approximation precludes computing the statistics of the motion, because all variability has been averaged out; nor can it be used in the case, treated below, in which the stators can move. Thus Eq. 7 cannot be used in all circumstances, and so the rotor motion must be computed directly from Eqs. 1–4 or the corresponding Fokker-Planck equations.

Stationary state occupancies

Equation 7 can be further approximated by assuming that the state occupancy probabilities, $p_i(\theta)$, are constant, independent of the rotor speed:

$$\langle \tau_m \rangle \approx \sum_{i=1}^{4} \int_0^{2\pi} p_i(\theta) \tau_M(\theta) \mathrm{d}\theta \tag{9}$$

This approximation applies when the motor is moving slowly enough that the protons' occupancy distributions are close to their steady-state values.

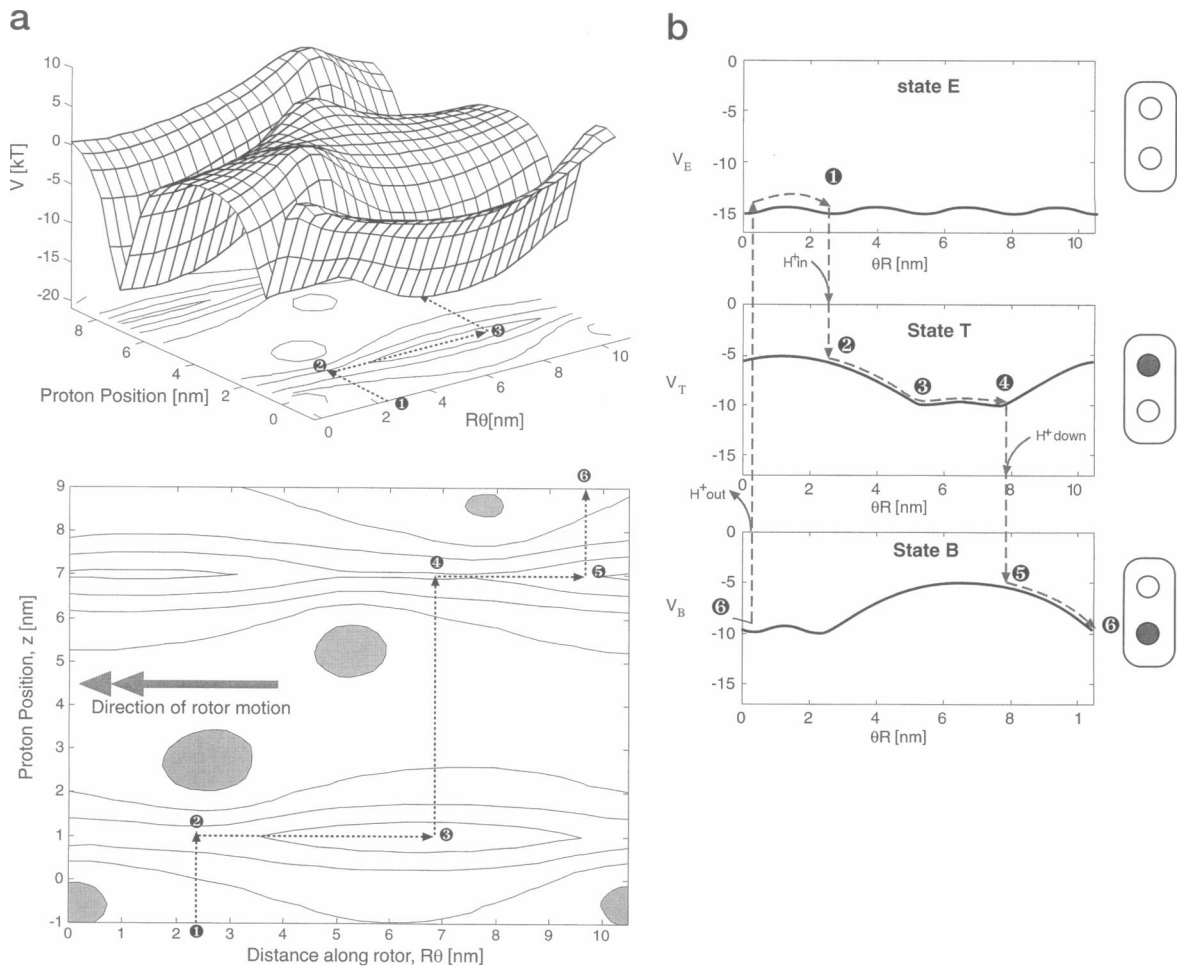

FIGURE 5 (*a*) Electrostatic potential field seen by a proton as it passes through the stator. The field was computed as a shielded Coulomb potential set up by the point charge distributions shown in Fig. 3 (cf. Appendix A). The top panel shows the potential profile as a function of the proton position in the stator and the distance along the rotor periphery, $R \cdot \theta$. The bottom panel is a projection of this surface onto a contour plot. The dashed line shows the path an observer riding with the proton would see as the rotor turns (i.e., moves to the left in this projection). When the rotor moves the top blocking charge out of the way, a proton in the periplasmic space at position 1 hops onto the top stator site 2. As the rotor turns, the proton is constrained to remain within the stator, and so it effectively moves along the valley of the potential until, at position 3, the second rotor blocking charge moves out of the way and the proton can hop to the lower stator site at 4. The rotor continues to move, forcing the proton to move along the valley of the second site potential until the lower blocking site is out of the way, whereupon it can hop off the stator into the cytoplasmic space. At each stage, the helical geometry of the rotor blocking charges steers the proton along the stator sites, and the electrochemical potential ensures that this random walk is biased downward. (*b*) Panels *A–D* trace the path of a point on the rotor as it is driven by the potentials $V_i(\theta)$ corresponding to each of the stator states (state F is not shown, because in this state there is no electrostatic coupling between rotor and stator). In position 1 the rotor is in equilibrium at a local minimum of the electrostatic potential corresponding to state E (stator empty). A small thermal fluctuation rotates it to position 2, where the upper blocking charge has moved to allow a proton to jump into the upper stator site. This neutralizes the charge site, and the potential switches to that corresponding to state T (top site occupied). After the jump 2 → 3, the rotor moves down the electrostatic gradient 3 → 4 to a local minimum. Another small thermal jump is required to move the rotor from position 4 → 5. This moves the lower blocking charge out of the way, allowing the proton to jump to the bottom site, 5 → 6, which switches the potential to state B (bottom site occupied). In state B the rotor again moves down the electrostatic gradient to position 7; a thermal jump then carries the rotor from position 7 (= position 1), which moves the lowermost blocking charge out of the way, allowing the proton to exit to the cytoplasm. Thus horizontal transitions are thermally excited motions of the rotor, and vertical transitions are thermally excited proton jumps.

In all cases the validity of these two assumptions must be checked numerically. In Appendix B we demonstrate the range of validity of both approximations.

RESULTS

In the Appendices we present a more complete description of the mathematical equations and the numerical methods employed in the simulations. The parameters employed in the simulations are given in Tables 1 and 2. An examination of the state occupancies as a function of rotation speed shows that if the upper and lower stator charges are exactly equal, then the proton spends most of its time in the upper state. Motor efficiency increases substantially if both states contribute more equally to torque generation, and so in the simulations we have made the top potential somewhat shal-

TABLE 1 Parameter values used in the simulations

Symbol	Meaning	Typical value
A	Cross-sectional area of the channel	1 nm^2
c_ℓ	Lumenal proton concentration	10^{-5} protons/nm^3
c_C	Cytoplasmic proton concentration	10^{-7} protons/nm^3
D_p	Free proton diffusion coefficient	10^9 nm^2/s
D_r	Rotor diffusion coefficient (free swimming)	20 radian^2/s
	Rotor diffusion coefficient (tethered)	0.7 radian^2/s
D_s	Stator diffusion coefficient	4×10^4 nm^2/s
E	Membrane potential	160 mV
k	Elastic constant of the stator	1–15 pN/nm
k_BT	Boltzmann's constant × absolute temperature	4.2 pN-nm
L	Length of the MotA/MotB channel	8 nm
$q^2/(4\pi\varepsilon_0)$	Electrostatic constant	230 pN-nm^2
ε	Dielectric constant	2–10
λ	1/electric screening distance	0.28 nm^{-1}

lower than the bottom to equalize the contributions of each site (cf. Table 2).

The behavior of the model is summarized in Figs. 6–10. We first examine the behavior of the fixed stator model shown in Fig. 3. Later we will remedy certain unsatisfactory aspects by allowing the stator to move and by adding fixed charges to the rotor-stator assembly. The data for both models are shown in the figures.

Fig. 6 shows a sample path for the rotor trajectory. Because there are only a few stator charges, when the proton jumps between sites the rotor torque is generated in discrete impulses. For the charge geometry shown in Fig. 3, each proton takes three hops to traverse a stator; each hop generates an impulse when a site is covered or uncovered. Thus when only one or two stators operate, the rotor appears to advance stepwise (cf. Fig. 10), but when eight stators operate the motor runs more smoothly.

Fig. 7 shows the basic mechanical behavior of the model (compare with Fig. 2). The load-velocity curve shown in Fig. 7 *a* is essentially linear for negative loads (i.e., loads that resist the motor's forward motion). The gray line through the origin is the "broken motor" curve, $\zeta_R\omega_B = \tau$. We can obtain a normalized motor torque by subtracting the broken motor curve from the active motor curve and normalizing by the zero-load velocity, $\omega_0 \equiv \omega(\tau = 0)$: $\omega_{REL} \equiv (\omega - \omega_B)/\omega_0$. Fig. 7 *b* shows the relative torque plotted

TABLE 2 The interaction amplitude, Λ, in units of k_BT between a proton and the rotor and stator charges

	Rotor	Stator-top	Stator-bottom
Λ, motor	15	10	11.5
Λ, pump	11	7.3	9

The motor performed better when the bottom well was deeper than the top well, for that equalized the relative state occupancies. When driven in reverse as a pump, performance increased if this inequality was increased so as to mimic an "alternating access" mechanism. The electrostatic shielding length was set at λ(motor) = 0.28, λ(pump) = 0.24. Λ is defined in equation A.10.

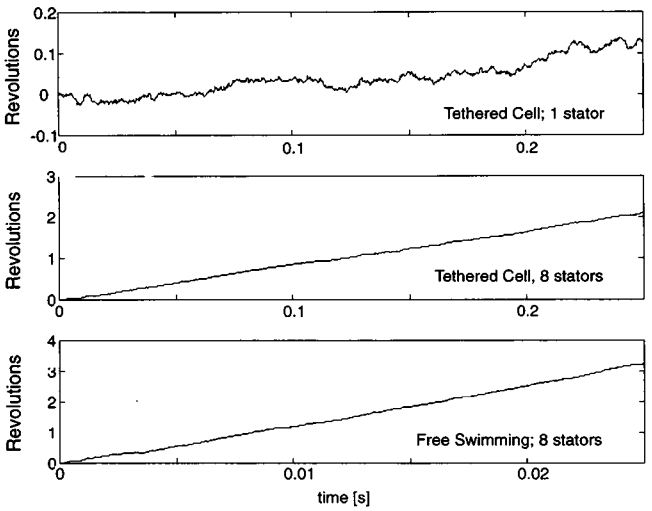

FIGURE 6 Stochastic simulation of a sample trajectory. (*a*) With one stator operating, the stepping behavior is clear. (*b*) With eight stators operating, the motor runs quite smoothly. This simulation corresponds to a drag coefficient of the tethered cell and an average angular speed of 8.8 Hz. (*c*) The same as *b*, but for a free-swimming bacterium with a drag coefficient corresponding to that of the flagellum (cf. Table 1); the average speed is 130 Hz.

versus angular velocity. We see that the proton turbine does not fit these data particularly well in two respects: 1) the predicted motor torque curve falls off immediately for $\omega_{REL} > 0$ without the constant torque plateau seen in the data; 2) the curve does not fall as low as the measured curve before leveling off.

Fig. 8 shows how the motor responds separately to the pH difference and to the potential difference across the membrane. Steady-state approximations were used to generate this figure. Varying ΔpH and $\Delta\psi$ separately shows that the dependence of velocity on ΔpH and $\Delta\psi$ is roughly equivalent. However, $\Delta\psi$ decreases in effectiveness as pH increases, because there are fewer protons to push through the motor. Furthermore, the velocity increases almost linearly with $\Delta\psi$, whereas the dependence on ΔpH is somewhat sigmoidal. (This could explain the observation that it is difficult to artificially energize swimming cells by a pH gradient alone (−75 mV) (S. Khan, personal communication.) The membrane potential has two effects: 1) it increases the proton gradient across the membrane by creating a Boltzmann increase at the top and a decrease at the bottom, and 2) if the electric field can penetrate the channel, it biases the proton's hops between states T and B. In Fig. 8 *a* we have assumed that the field can penetrate the channel; Fig. 8 *b* shows the same situation with a nonpenetrating field.

The motor speed increases almost linearly with PMF (data not shown), in accordance with experimental observations. Fig. 9 shows that the proton flux through the motor increases almost linearly with speed until saturation at high velocities. The smooth-running approximation was used to

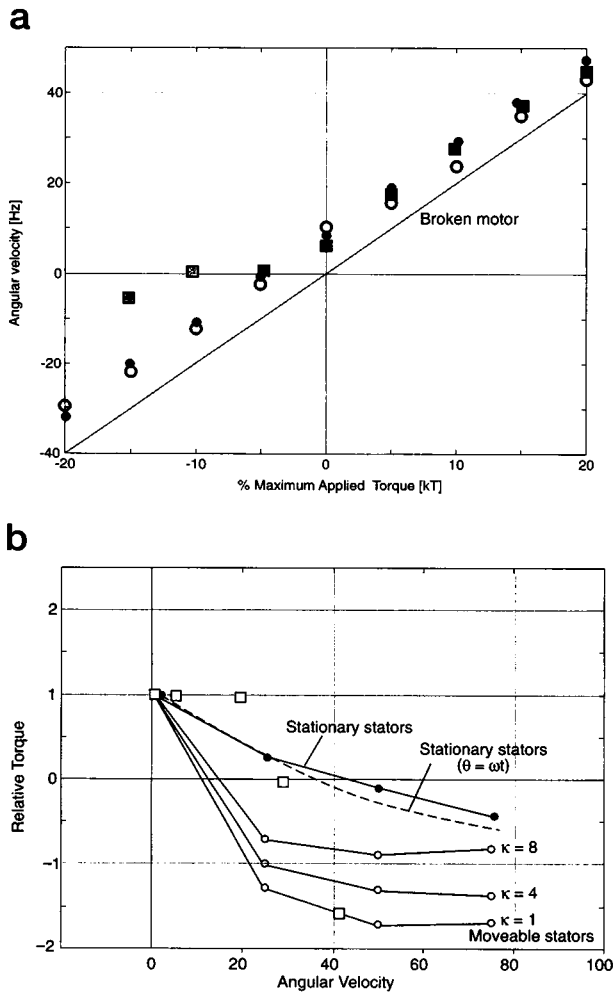

FIGURE 7 (*a*) Load-velocity curve. ●, Fixed stator model; ○, movable stator model; ■, data from Berg and Turner (1993). The gray squares indicate dubious data points, showing a barrier to reverse rotation (cf. Fig. 2). The model does not exhibit any barrier to driving the motor in reverse. (*b*) Angular velocity, ω, versus relative motor torque $\omega_{REL} = (\omega - \omega_B)/\omega_0$, where ω_B is the broken motor velocity and ω_0 is the no-load velocity (cf. Fig. 2). The top (*solid*) curve is the stationary stator; the dashed line is the smooth-running assumption: $\theta = \omega t$. The lower three solid lines are the moving stator model for three values of the elastic constant, κ. The data (from Berg and Turner, 1993), at 22°C, are indicated by squares. Note that neither version of the ion turbine model can match the plateau region below $\omega \approx 200$ Hz, nor can the linear drop thereafter to a saturating lower value.

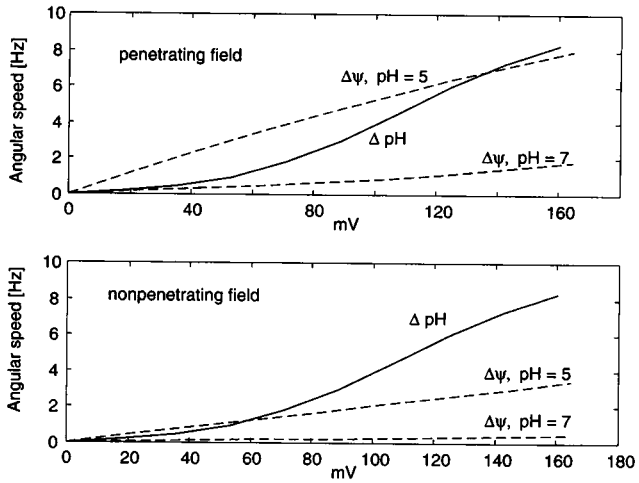

FIGURE 8 Motor behavior as a function of membrane potential and pH gradient (in mV). For this figure we have assumed that the probabilities for the stator occupancies are given by their steady-state values, and that the mean torque can be computed from Eq. 9. We have checked that, for this simulation, the approximation is valid (cf. Appendix B). (*a*) For a ΔpH 2, the increase in motor speed with $\Delta\psi$ is almost linear, and the dependence on pH is somewhat sigmoidal. The effectiveness of $\Delta\psi$ decreases as pH increases, because there are fewer protons available to drive the motor. (*b*) The same situation as in *a*, but the field cannot penetrate the membrane, and only builds up a Boltzmann enhancement of protons at the entrance and depletion at the exit, thus raising the effective ΔpH across the stator. The motor speed increases nearly linearly with $\Delta\psi$ at a fixed bulk ΔpH 2, but the dependence on $\Delta\psi$ is the same as in *a*.

compute this figure. The proton flux was computed from

$$J_P = \frac{1}{T}\int_0^T [(k_{ET}p_E - k_{TE}p_T) + (k_{BF}p_B - k_{FB}p_F)]dt \quad (10)$$

At $\omega = 100$ Hz, the proton flux is $\sim 2 \times 10^4$ s^{-1}. This is somewhat lower than the observed flux of $\sim 10^5$; however, some proton leakage, or more than eight working stators, would increase the flux to the observed value. The initially linear behavior of Fig. 9 gives the impression that, for most of its range, the motor is "tightly coupled" to the proton flux, because a fixed number of protons pass through the stators per revolution. Fig. 9 *b* shows that the motor speed at constant load increases nearly linearly as the number of active stators increases, except for one or two stators. This discrepancy is an artifact due to the "Vernier effect" of placing the stators almost periodically around the rotor. Later, when we allow the stators to move elastically, this effect will disappear.

As Fig. 6 *b* illustrates, when more than two or three stators operate, the motor runs quite smoothly. Samuel and Berg (1995) used first-passage time statistics to ascertain that the *E. coli* motor behaved as a stepper. Fig. 10 shows a plot of the log of the variance for a fixed number of rotations versus the log of the motor speed. A constant torque motor will have a slope of -3, whereas a "Poisson stepper" will have a slope of -2 (Samuel and Berg, 1995). The slope of the curve for a stationary stator is ~ -2.9, reinforcing the impression that it runs quite smoothly. The movable stator has a slope of -2.5, demonstrating that, even though many impulses are delivered to the rotor per revolution, the motor still retains some "stepping" behavior. (The analysis of first-passage time statistics for the bacterial flagellar motor is dealt with in detail by Wang et al. (manuscript in preparation).)

The ion turbine with movable stators

As the motor is driven forward by an external torque, at some point the driving torque exceeds the motor torque and

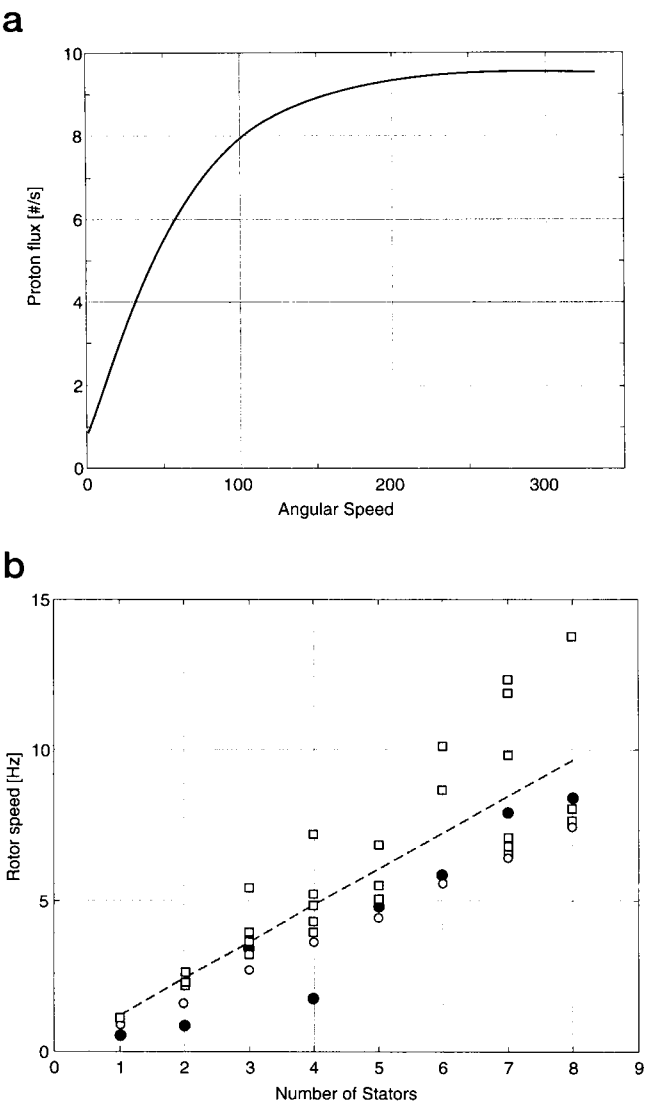

FIGURE 9 (*a*) Initially the proton flux increases nearly linearly with rotor speed, but ultimately saturates. (*b*) At constant load, angular speed (ω) increases linearly with the number of active stators (N). The dashed line is the smooth-running approximation ($\theta = \omega t$); ●, fixed stator; ○, movable stator; □, data from Samuel and Berg (1996). Note that the fixed-stator model exhibits linearity only for $N \geq 4$; this is due to the "Vernier effect" of placing the stators nearly periodically around the rotor. When the stators are allowed to thermally fluctuate, this effect washes out.

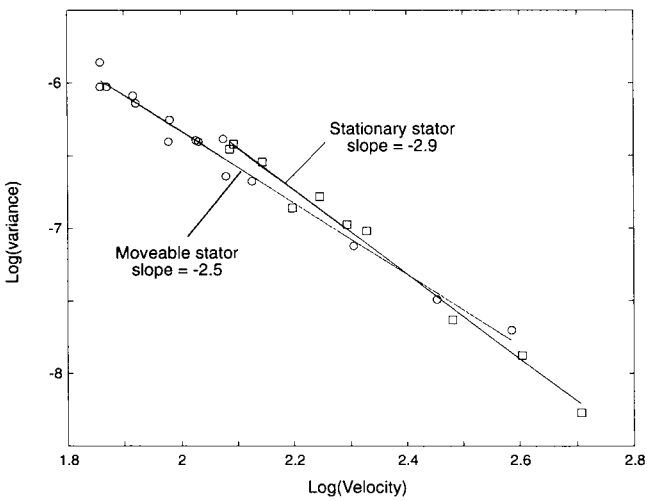

FIGURE 10 Evidence of stepping behavior. With eight stators operating, a plot of ln(var) versus ln(ω) for the stationary stator (○) gives a slope of −2.9, close to the smooth-running slope of −3 expected from a constant-torque motor. Allowing the stators to move against an elastic element of strength 4 pN/nm produces a slope of −2.5 (□) intermediate between the slope of −3 expected from a constant torque motor and the slope of −2 expected from a pure "Poisson stepper."

the motor commences to act as a brake on the driving torque. This causes the curve in Figs. 2 *b* and 7 *b* to bend over, eventually become negative, and finally level off. This trend is much more pronounced in the experimental data (Fig. 2 *b*) than in the model (Fig. 7 *b*). A second discrepancy between the model's performance and experimental observations is seen in the first-passage statistics (cf. Fig. 10): the stationary stator model indicates a smooth-running motor. One way to remedy these deficiencies is to permit the stator some freedom to move. This is reasonable, because MotB is anchored to the peptidoglycan layer (but no such anchoring has been demonstrated for the four MotA helices). Because no such anchor can be perfectly stiff, we allow some elasticity in the stator and consider the modification of the turbine model shown in Fig. 11 *a*. The stator acts as before, but it is anchored by a linear elastic element. This introduces a second dynamic equation for each stator. For simplicity, we shall assume that the stator can move only tangentially to the rotor. This results in a Langevin equation of the same form as Eq. 4:

$$\zeta_S \frac{dx}{dt} = -\frac{\partial}{\partial x} V(\theta, x, t) + f_S(t) \qquad (11)$$

where x is a coordinate tangential to the rotor. The potential now includes the elastic energy of the tether:

$$V(\theta, x, t) = V_{ELEC}(\theta, x, t) - \kappa(x - x_0)^2, \qquad (12)$$

where V_{ELEC} is the electrostatic potential as before, κ is an elastic constant, and x_0 is the rest length of the tether. A more realistic model would permit motion in two or three dimensions. The Brownian force, $f_s(t)$, is uncorrelated with the corresponding term in the rotor equation.

Fig. 11 shows the rotor and stator motions for tethered cell conditions. The stator fluctuates about its mean position (Fig. 11 *b*), which is offset from its equilibrium position in the direction opposite the rotor motion (Fig. 11 *c*). Fig. 7 *b* (*open circles*) shows the effect of this modification on the motor torque: the curve bends over more quickly and falls to a lower value than when the stator is rigid (i.e., when $\kappa x_0^2 \gg k_B T$). The reason for this is that the time scale needed for the rotor to move under the elastic force of the stator is $\tau \approx \zeta_R/\kappa$ (Kleutsch and Laüger, 1990), so that when the rotor is driven faster than this time scale, the stators can no longer transduce force efficiently and the stator commences to brake the rotor. This time scale is considerably

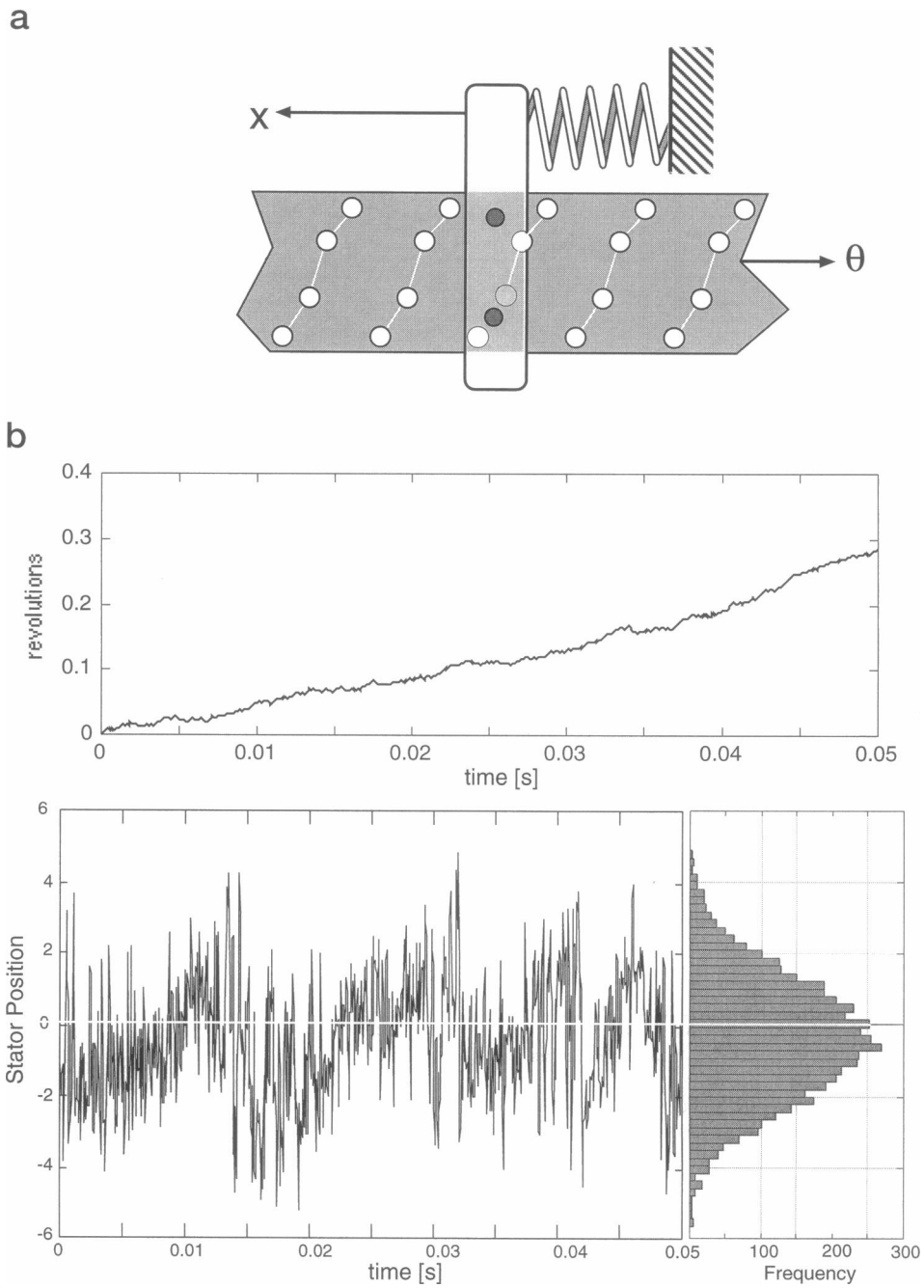

FIGURE 11 (*a*) The ion turbine model with a movable stator. The stator is anchored to the peptidoglycan layer via MotB. We model this as a linear spring with elastic constant κ. The stator can move only horizontally tangential to the rotor along the x coordinate. (*b*) The top panel shows a rotor trajectory with eight flexible stators. The middle panel shows the stochastic motion of the stator as it fluctuates about its mean position. The distribution of stator positions to the right shows that the mean position is offset from the equilibrium position in the direction opposite rotor motion.

longer than that for proton hopping, which is the rate-limiting step for the rigid rotor model.

The movable stator model does a better job of reproducing the motor torque data of Fig. 2 than the rigid rotor model. However, both models fall off smoothly for positive torques and do not exhibit the plateau region below $\omega \approx 100$ Hz. We shall suggest a remedy for this below. Fig. 10 shows that the elastic stator model produces a slope of -2.5 when the log of the variance in the first passage time is plotted against the log of the mean rotation rate. This is closer to the experimentally measured slope of -2, indicating more steplike behavior.

The effect of fixed rotor charges

Fig. 7 *b* shows that the movable stator fits the motor torque better than the fixed stator model. However, the pronounced plateau measured for small forward velocities is not present in either version of the model. To reproduce this feature of the data, we added a periodic potential to model fixed charges around the rotor that interact with the stator, even when the motor is de-energized. This introduces an electrostatic analog of "sliding friction" that resists small external torques, but has little effect at higher torques. This assumption is reinforced by the observation that de-energized mo-

tors appear to stall at quantized angles, suggesting a rotor-stator interaction that is present in the absence of any electrochemical potential. Fig. 12 shows that the movable stator with a fixed, periodic rotor-stator interaction improves the fit to the motor torque behavior by adding the plateau observed at speeds less than ~100 Hz. Addition of the periodic potential slows the average speed to ~5.5 Hz and adds a small barrier to reverse rotation.

The turbine as a pump

The flow of protons through the rotor/stator assembly has the character of an "alternating access" gated channel (Alberts et al., 1994), where the motion of the rotor acts as the conformational change that exposes the proton alternately to the lumenal and cytoplasmic environments. If an external torque is applied to the rotor, protons will bind to the bottom stator site and be forced upward to the top site, where they can dissociate into the lumenal space.

The pumping efficiency is greatly improved by making the bottom (cytoplasmic) stator potential well deeper than the top (periplasmic) well, for then the proton can bind tightly to the bottom stator site, but dissociate easily from the top stator site, which faces the higher proton concentration. Up to a point, this modification makes the motor operate more efficiently as well; however, if the charges are too unequal, the motor will not function. Table 2 gives the values we used in the simulation; Fig. 13 shows how the proton flux from the cytoplasm to the lumen depends on the rotor speed when driven in reverse. A similar mechanism may underlie the operation of V-type proton pumps (Alberts et al., 1994).

Reversing the motor

Wild-type flagellar motors spontaneously reverse their direction of rotation randomly with a frequency of ~1/s, with a slight bias toward counterclockwise rotation. These reversals cause the bacterium to alternate between "runs" and "tumbles," which randomly resets the direction of swimming. The bacterium implements its chemotactic response by varying the frequency of these reversals (Berg, 1983; Schnitzer et al., 1990). The model as formulated so far is unidirectional, and so must be modified to make reversals possible.

The most obvious method of changing the direction of rotation is by changing the slant of the rotor charges. This could be accomplished if the rotor were capable of the same

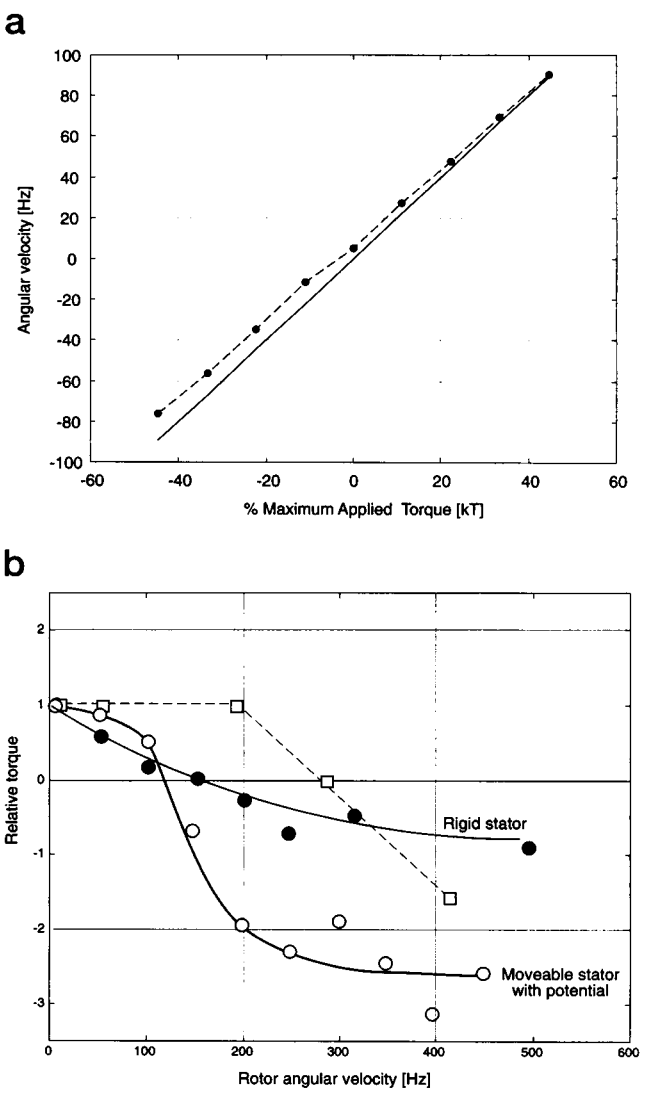

FIGURE 12 The movable stator with fixed charges that do not enter into torque generation. Ten stationary charges were placed around the motor periphery, modeled by adding a periodic potential of the form $(6k_BT)\sin^2(10\theta)$. (*a*) The load-velocity curve is nearly the same, but with a small barrier to being driven in reverse. (*b*) A relative torque plot shows a plateau region at small positive torques.

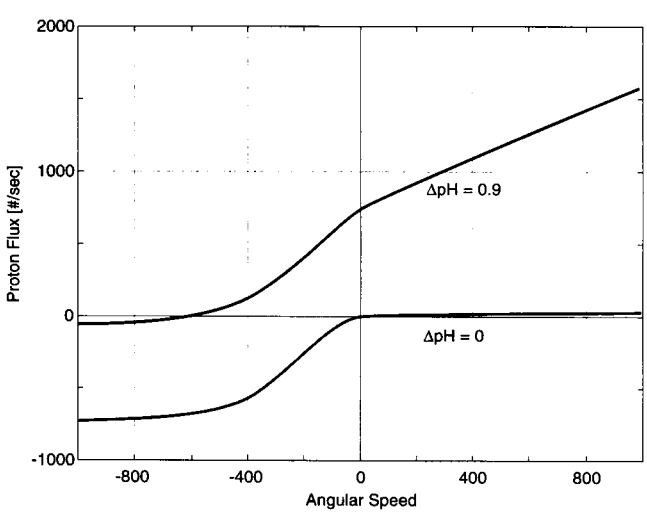

FIGURE 13 The motor can act as an effective proton pump. The figure shows the proton flux, J_P, computed from Eq. 10, as a function of rotor speed, ω, when the rotor is driven by an external torque, τ. If the top well is reduced to ~80% of the bottom well, the motor can pump against a $\Delta pH \approx 1$.

kind of twist reorientation that characterizes the opening and closing of gap junctions (Alberts et al., 1994). This type of global conformational change would reorient all of the charge tilts simultaneously with respect to the stator, and thus reverse the direction of rotation. The free energy needed to initiate this switch could come from the binding free energy of phosphorylated CheY to the rotor (Tang et al., 1996; Zhao et al., 1996). Back-switching would be triggered by dephosphorylation of CheY and its dissociation from the rotor. This mechanism is shown in Fig. 14. Naber (1996) showed that a mechanism of this sort could account for the statistics of switching in *Halobacterium salinarium* (Naber, 1996).

A more subtle mechanism for reversing the direction of rotation takes advantage of the "alias" helix. If the pattern of rotor charges has some helical symmetry, then there can be a secondary helical charge path analogous to the helical patterns found in plant phyllotaxis (Douady and Couder, 1992). This secondary helix can be transformed into the primary proton path by the binding of CheY, which, because of its negative charge, could convert one of the positive rotor charges to a negative charge capable of providing a proton-binding site. We will investigate the switching behavior of the model in a subsequent publication (Elston and Oster, manuscript in preparation).

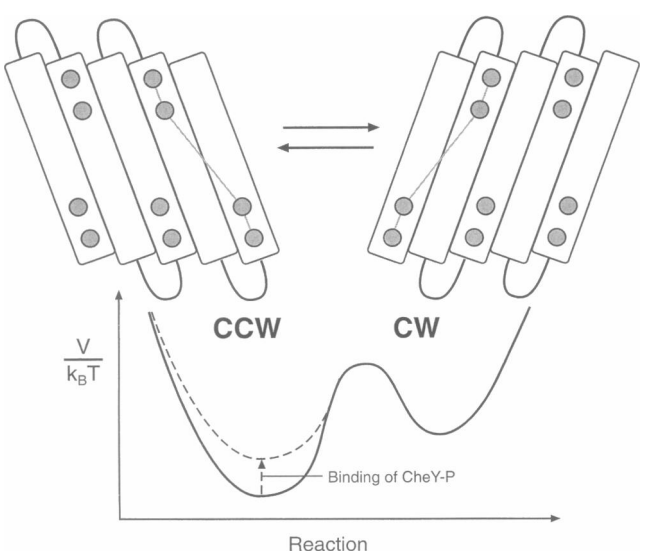

FIGURE 14 A possible mechanism for reversing the direction of rotation for the turbine model. If the stator charges were organized as repeated subunits, analogous to transmembrane α-helices, then the rotor charges could have two conformations of opposite tilt. If the counterclockwise (CCW) conformation were the most stable, then the motor would default to CCW rotation, with stochastic switching to clockwise (CW) rotation. The switching rate constants can be modeled by Kramers transitions (Appendix A). Successive binding of phosphorylated CheY to the rotor (FLiM, FliN) could decrease the depth of the CCW potential well until the cooperative switching to CW rotation is triggered.

COMPARISON WITH OTHER MODELS

It is frequently difficult to compare different models when they are expressed in different mathematical formalisms, and when they appear to spring from different physical, chemical, and/or biological assumptions. The model we have described here resembles in certain respects several earlier models; in particular, the "ion turbine" model first proposed by Laüger (1977), and the "gumball machine" proposed by Berg and Khan (Berg and Khan, 1983; Meister et al., 1989). These models were formulated as discrete-state Markov chains, whereas the mathematical formulation we have pursued here stems from nonequilibrium statistical mechanics. The virtue of expressing the model in this fashion is that it makes clear the underlying physics, and it allows us to see more clearly the similarities and differences between the three models.

Laüger's original model postulated that protons were restricted to moving along the intersection of continuous "half-channels" located on the rotor and stator (Laüger, 1977). He did not offer a specific mechanism for this kinematic restriction, and he formulated the model as a spatially discretized Markov chain. Mechanical forces entered only as Boltzmann factors in the thermally activated jumps between states. Because of his spatial discretization, his model was essentially a biased random walk on a lattice formed by the possible intersection points of the rotor and stator half-channels. Progress of the rotor depended on a coincidental fluctuation wherein the proton jumps to the next site downward and the rotor fluctuates to the next site forward. The proton gradient ensures that this is a more likely event than the other three possible jumps. In a subsequent treatment, Kleutsch and Laüger permitted the stator to diffuse on a discrete lattice against an elastic tether (Kleutsch and Laüger, 1990), but they did not treat diffusion of the rotor; consequently, the model could produce no torque if the tether became rigid. Berry generalized Laüger's model by taking into account the electrostatic coupling between rotor and stator and by treating the rotor motion continuously (Berry, 1993). Berry did not allow the stator to move; moreover, he also assumed, as did Laüger, that the rotor moved smoothly (i.e., $\theta = \omega t$ at all speeds ω). Our simulations have shown that this is not always the case, and for the parameters used in this paper, the assumption only becomes valid when several stators are operating. This assumption also precludes computing motor statistics such as the first-passage time distributions, which provide information on the force-generating mechanism (Samuel and Berg, 1995).

Berg and Khan formulated a model that appeared quite different from either Laüger's or Berry's (Berg and Khan, 1983). They postulated "half-channels" that forced the proton to travel part way through an elastically tethered stator. When the stator fluctuated in one direction sufficiently to align with a half-channel on the rotor, the proton jumped from the rotor to the stator and held the two together until the stator's elastic tether pulled the rotor back toward the

stator's rest position. Because they did not offer a specific electrostatic picture, they had to impose kinematic constraints on the directions in which the stator could fluctuate. In a subsequent mathematical treatment, Meister et al. formulated the model as a discrete Markov chain and showed that it functioned as a "thermal ratchet" analogous to Huxley's original model for the myosin head: the stators' thermal fluctuations were rectified by proton binding to the rotor, which produced an elastic torque on the rotor (Huxley, 1957; Meister et al., 1989). As in the Kleutsch-Laüger model, making the stators rigid greatly reduces torque generation, because it then depends on rotor fluctuations.

In some respects, our fixed stator model resembles Berry's, and our movable stator model resembles the model of Berg and Khan. However, the resemblance is more in the motor geometry than in the mechanism of torque generation. The Kleutsch-Laüger and Berg-Khan models derive their torque from elastic forces generated by rectifying the thermal diffusion of the stators. The reason for allowing the stator to move was to take advantage of the faster thermal diffusion of the stator as compared to the much larger rotor. Like Berry's model, torque generation in our fixed-stator model arises from electrostatic forces; our movable stator model generates torque by a combination of electrostatic and elastic forces. (In computing the transition rates between stator states, we use Kramers theory and the electrostatic barrier heights separating the potential wells. In contrast, Berry scales the differences in potential well depths (i.e., pK values) to compute transition rates. This produces the correct equilibrium probabilities, but the transition rates cannot be computed in this fashion.) Our model depends on thermal energy to excite the proton hops between stator charges; however, force generation arises principally from electrostatic forces, so allowing the stator elastic constant $\kappa \to \infty$ actually increases the motor torque. Thus the inclusion of unavoidable protein elasticity embodied in the stator elastic constant, κ, improves the fit to the motor torque data in Fig. 2, but it does not improve the mechanical behavior of the motor. This difference is discussed in more detail in Appendix C.

Another difference between our model and the Kleutsch-Laüger and Berg-Khan models is buried in the different mathematical formulations. In the discrete-state model formulations, mechanical forces are incorporated as Boltzmann factors in the transition probabilities between stator positions and by permitting the rotor to relax in discrete increments under the elastic forces of the stators. This spatial discretization increases the apparent coupling between the rotor and stator; its effect on other aspects of motor function can be investigated by using the Langevin-Markov formulation we have employed here.

Finally, in our model the geometry of the charge distributions replaces "half-channels" and makes the imposition of kinematic constraints on the stator motion unnecessary. That is, we do not impose any constraint on the stators' or protons' motion other than that dictated by elastic and electrostatic forces. Furthermore, we do not require that protons bind to the rotor, which is an essential feature of the Berg-Khan mechanism. The forces enter explicitly (as described by Eq. 4) as an electrostatic-elastic potential, $V(\theta, x, t)$ (Eq. 12) and the Brownian forces, $f_R(t), f_S(t)$. This makes the mechanism of force transduction clear, and the relationship between these mechanisms is more transparent.

DISCUSSION

We have presented an electromechanical model for the bacterial flagellar motor based on the notion that the flow of protons through the system upsets the electrostatic equilibria between the rotor and stator. The protons' thermal energy permits them to jump between the fixed acidic charge sites, and the electrochemical gradient between the periplasmic space and the cytoplasm biases this hopping down the gradient. The thermal energy required to jump between sites is transduced into the electrostatic energy that drives the rotor. Thus the electrochemical energy of the protons (the ultimate energy source) is converted first to binding free energy of the proton to the acidic sites. Thermally driven jumps then convert this binding energy into an electrostatic torque. The magnitude of this torque depends on several parameters in the model; two major factors are 1) the number, spacing, and depth of the potential wells along the proton conduction path, i.e., the pK_a's of the amino acids that form the sites. (The pK_a's are related to the well depths approximately as $2.3 \cdot pK_a \approx V/k_BT$; however, the pK_a's of sites internal to the protein may be quite different from those determined by solution titration. Nevertheless, the residue pK_a's of aspartate (3.65) and glutamate (4.25) are in the correct ranges ($8.4–9.77k_BT$).) These determine the strength of the electrostatic impulse accompanying each proton hop. 2) The dimensions and dielectric constant of the stator and its distance from the rotor. We have used a rotor-stator distance of ~0.7 nm; reducing this will increase the strength of the motor.

There are many patterns of rotor and stator charges that can generate torque; what is necessary is that the thermally driven hopping of protons (or sodium ions) between fixed sites alter the electrostatic interaction between the rotor and stators such that a unidirectional torque is generated. This requires that the charge distribution geometry contain a helical component consisting of negative protonation sites and positive gating sites. We have placed this component entirely on the rotor, but this is not necessary. Moreover, we have separated the positive and negative fixed charges so that the rotor is completely positive and the stator negative. This is also unnecessary: a distribution that permits the rotor and stator to carry charges of both signs is permissible as long as the helical component to the proton's path is maintained. Recent work places both positive and negative sites on both FliG (rotor) and MotA (stator); such an arrangement can be accommodated by the mechanism we have proposed here (Lloyd and Blair, 1997; Tang et al., 1996).

We have made the top stator fixed charge smaller than the bottom charge for two reasons. First, it increases the mo-

tor's efficiency by making residence times of the proton in the two sites more equal to each other, so that the two sites contribute equally to torque generation. Second, this arrangement permits the motor to act as an ion pump when driven in reverse. When the rotor is driven in reverse by an external torque, protons bind tightly to the lower stator sites and are driven upward by the rotor motion, which creates an upward electrostatic field gradient. Once in the top site, they easily dissociate into the periplasmic space. Thus the motion of the rotor acts as the conformational change associated with "alternating access" ion pumps (Alberts et al., 1994). This mechanism may operate in F- and V-type ATPase ion pumps.

The amino acid sequence of MotA has been determined (Dean et al., 1984). Sharp et al. examined MotA by tryptophan-scanning mutagenesis and found no continuous path of hydrogen bonds that could provide a "proton wire" to conduct protons from the periplasmic space to the cytoplasm (Sharp et al., 1995a), and so they concluded that there must be a central water channel to provide a proton pathway. However, the mechanism described here does not require a continuous proton path; indeed, the proton turbine would not work well if such a path were present, because the mechanochemical transduction from $\Delta\tilde{\mu}$ to torque depends on the thermal hopping of the protons between separated sites. This very possibility is admitted by Sharp et al., provided the proton pathway is formed from several MotA helices (Dean et al., 1984).

Finally, the energy transduction mechanism we have described here can, with some modification, be applied to other mechanochemical proteins. In particular, we shall investigate how this principle can be applied to explain certain aspects of ATP synthase, and F- and V-type ion pumps (Elston et al., manuscript in preparation).

APPENDIX A: DYNAMICAL EQUATIONS FOR THE ION TURBINE MODEL

In this appendix we describe in more detail the mathematical model for the proton turbine.

Proton motion

To describe the motion of a proton through the stator, we could explicitly track its trajectory by writing a Langevin equation:

$$\zeta_p \frac{dz}{dt} = -\frac{d}{dz} V(z, x, \theta) + f_p(t) \qquad (A1)$$

where $\zeta_P = D_P/k_BT$ is the drag coefficient of the proton, and $V(z, x, \theta)$ is the field due to the electrostatic interactions with the rotor, stator, and the membrane potential. A difficulty with this formulation is that it is unclear how to incorporate the concentration gradient across the membrane as boundary conditions on Eq. A.1. (One approach is to mimic the different reservoir concentrations by Poisson sources of different strengths at $x = 0$ and $x = L$. But there is no analytical demonstration that this gives correct solutions under all conditions.) To remedy this difficulty, one can model the proton motion by the corresponding Fokker-Planck diffusion equation for $c_P(z, \theta, t)$, the concentration of protons at position z in the stator at time t (or, normalizing by integrating over z, the probability of finding a proton at position z at time t):

$$\frac{\partial c}{\partial t} = D_p\left\{\frac{\partial^2 c}{\partial z^2} + \frac{1}{k_BT}\left[\frac{\partial}{\partial z}\left[\frac{\partial}{\partial z} V(z, x, \theta)\right]c\right]\right\} \qquad (A2)$$

Equation A.2 is solved subject to the boundary conditions $c(0)$ and $c(L)$, the concentrations of protons in the lumen and cytoplasm, respectively (L is the length of the stator). (Note that Eq. A.2 does not include charge repulsion between protons; to incorporate this a nonlinear term proportional to $c(z)$ $\int_0^L \Phi(z, z')c(z')dz'$ must be added, where Φ is the interaction potential between two protons.)

In principle, knowing the charge distributions, one can solve this equation simultaneously with the appropriate equations for the rotor and stator to obtain the proton probability distribution. However, in practice this is generally not possible, because of the widely disparate time scales of the rotor and proton motions. The characteristic time scales for the motions of the proton, stator, and rotor can be estimated from their respective diffusion constants as $\tau \approx$ diffusion coefficient/(characteristic length)^2. If we take the characteristic length as $L \approx 10$ nm, the length of the stator, then the time scales are in the proportions

$$\text{proton:stator:rotor} = 10^7{:}10^2{:}10^{-1}[s^{-1}] \qquad (A3)$$

This wide disparity in time scales makes some type of approximation necessary, because following the protons' motions simultaneously with the rotor motion would require a very small integration time step.

Thus on the scale of the rotor's motion, the protons in the stator spend nearly all of their time associated with their binding sites, and a negligible time diffusing between sites. Therefore, if the binding sites are relatively deep compared with k_BT, it is sensible to approximate the proton motion by a Markov chain that simply keeps track of the residence times the proton spends in discrete stator "states." These states are determined by the location of the charges on the rotor and stators. Jumps between the states will be considered instantaneous on the time scale of the rotor motion, and the rate at which these jumps occur will be determined by the method of Kramers (Hanggi et al., 1990). It is not a trivial task to derive the Markov equations rigorously from Eqs. A.1 or A.2, and so we must justify the approximation heuristically.

In Kramers' theory the transition rate between a state located at $z = a$ over a potential barrier located at $z = b$ is approximated by

$$[\text{jump rate from } x = a \text{ to } x = b] \equiv k_{ab}$$

$$\approx \frac{D_p}{2\pi k_BT}\sqrt{V''(a)|V''(b)|}\,e^{-[V(b)-V(a)]/k_BT} \qquad (A4)$$

Here D_p is the diffusion coefficient of a proton, and $\Delta V = V(b) - V(a)$ is the height of the potential barrier separating the two states (ΔV includes the membrane potential, $\Delta\psi$). The quantity in the square root measures the effect of the well width on the jump rate.

Because the form of the real potential is not known in explicit detail, we will approximate k by

$$k \approx \frac{D_p}{\Delta z^2} e^{-[\Delta V]/k_BT} \qquad (A5)$$

where $\Delta z = 3L/8$, half the distance between binding sites, and ΔV is the height of the electrostatic potential separating the two states. (Note that the dimensions of $(1/2\pi k_BT)\sqrt{V''(a)|V''(b)|}$ is (length)^2; we have chosen our length scale as the distance, Δz, between stator binding sites.) This approximation also has the advantage that it ensures the probabilities that the top and bottom states satisfy the Boltzmann equilibrium conditions. The depth of the potential well can be estimated from the pK_a of the titratable amino acid sites (e.g., arg and/or glu on the stator): $\Delta V \approx 2.3k_BT\,pK_a$.

The jump rates at which the protons enter the stator from either end must be handled differently, for they depend on the concentration (i.e., pH)

in the periplasmic space and the cytoplasm. We model the jump rates for protons entering the channel from the periplasmic space by

$$k_{in} \approx \frac{cAD_p}{\Delta z} e^{-[\Delta V_e]/k_B T} \tag{A6}$$

where c is the concentration in the periplasmic space, ΔV_e is the potential drop across the channel entrance, and A is an effective cross-sectional area. A similar expression governs the entrance rate from the cytoplasm.

Using these expressions for the transition rates, we can write the transition matrix for the four-state Markov chain governing the stator site occupancies as given in the text.

Note that the membrane potential influences the proton dynamics in two ways. First, if the dielectric constant of the stator is low, the field could penetrate the protein and bias the proton jumps between the internal sites T and B. Second, even if the field cannot penetrate the stator, it will build up a Boltzmann concentration profile at the stator entrance and a similar Boltzmann depletion profile at the stator exit. Therefore, the ΔpH across the stator will be greater than indicated by the measured bulk pH's in each compartment. We have simulated the effect of each of these alternatives on the motor performance.

Rotor and stator motion

We begin with the mechanical Langevin equations for the rotor driven by a single elastically tethered stator. The Langevin equations for the motion of the rotor and stator are

$$\zeta_R \frac{d\theta}{dt} = -\frac{\partial}{\partial \theta} V(x, \theta, t) + \sqrt{2k_B T \zeta_R} f_R(t) \tag{A7}$$

$$\zeta_S \frac{dx}{dt} = -\kappa x - \frac{\partial}{\partial x} V(x, \theta, t) + \sqrt{2k_B T \zeta_S} f_S(t) \tag{A8}$$

where θ is the angular coordinate of the rotor and x is the position of the stator tangent to the rotor. κ is the elastic constant of the stator, and the time dependence in the potential, $V(x, \theta, t)$, is governed by the Markov process for the protons. The electrostatic force on the rotor and stator is computed from the electrostatic potential, $V(x, \theta, t)$, as

$$\mathbf{F}(x, \theta, t) = -\frac{\partial}{\partial x} V(x, \theta, t) = \frac{1}{R} \frac{\partial}{\partial \theta} V(x, \theta, t) \tag{A9}$$

The interactions between the rotor and stator charges are governed by screened Coulomb potentials. That is, for two point charges, V is given by

$$V(\mathbf{r}, \mathbf{r}') = \Lambda \frac{e^{-\lambda|\mathbf{r}-\mathbf{r}'|}}{|\mathbf{r} - \mathbf{r}'|} \tag{A10}$$

where $\Lambda = q^2/(4\pi\hat{\varepsilon})$ is the electric coupling strength, λ is the screening distance and $\hat{\varepsilon}$ is the dielectric constant. (In a vacuum, $\Lambda \approx 230$ pN-nm^2; assuming a dielectric constant inside the stator of 2–10, $\Lambda \approx 23$–115 pN-nm^2.)

Let $X = R\theta$ be the linear distance along the rotor periphery, and define the following dimensionless variables:

$$x' = \sqrt{\frac{\kappa}{k_B T}} x, \qquad X' = \sqrt{\frac{\kappa}{k_B T}} X, \qquad t' = \frac{k}{\zeta_x} t \tag{A11}$$

and let

$$\zeta_x = \frac{\zeta_R}{R^2}, \qquad \varepsilon = \frac{\zeta_S}{\zeta_R}, \qquad V' = \frac{V}{k_B T}, \qquad \tau'_{appl} = \frac{\tau_{appl}}{\sqrt{\kappa k_B T R}} \tag{A12}$$

Then the equations in dimensionless form are

$$\text{Rotor:} \quad \frac{dX}{dt} = \varepsilon\left(\frac{\partial}{\partial x} V(X - x, t) + \tau_{appl}\right) + \sqrt{2\varepsilon} f_R(t) \tag{A13}$$

$$\text{Stator:} \quad \frac{dx}{dt} = -x - \frac{\partial}{\partial x} V(X - x, t) + \sqrt{2} f_S(t) \tag{A14}$$

where τ_{appl} is the applied load force. For the case when the stator is rigid, $dx/dt \to 0$, it is convenient to scale the time to the rotational diffusion coefficient of the rotor: $t' = tD_R$. This leads to the following equation for the rotor:

$$\frac{d\theta}{dt} = -\frac{\partial}{\partial \theta} V(\theta, t) + \tau_{appl} + \sqrt{2} f_R(t) \tag{A15}$$

Fokker-Planck equations

In the simulations presented in this paper, we have employed the Langevin equation formulation. To obtain good statistics one must run these simulations many times, or for long times. An alternative approach is to use the corresponding Fokker-Planck equations, which yield the probability distributions in one computation, albeit at the price of greater computational complexity. We include this formulation here for completeness; we will employ it in the companion paper.

Let $\rho(\theta, t)$ be the probability distribution function for finding the rotor at angular position θ at time t. Then ρ evolves according to the Fokker-Planck equation:

$$\frac{\partial \rho}{\partial t} = D_r\left\{\frac{\partial^2}{\partial \theta^2}\rho + \frac{\partial}{\partial \theta}\left[\frac{\partial}{\partial \theta} V_{RS} - \tau_{app} + A\int_0^L c \frac{\partial}{\partial \theta} V_{pr}\, dz\right]\frac{\rho}{k_B T}\right\}$$
$$+ D_s\left\{\frac{\partial^2 \rho}{\partial x^2} + \frac{\partial}{\partial x}\left[\left(\frac{\partial}{\partial x} V_{RS} + \kappa(x - x_0)\right.\right.\right.$$
$$\left.\left.\left. + A\int_0^L c \frac{\partial}{\partial x} V_{ps}\, dx\right)\frac{\rho}{k_B T}\right]\right\} \tag{A16}$$

where $c(z, t)$ evolves according to Eq. A.2.

Equation A.16 is solved subject to the boundary conditions

$$\rho(\theta, \pm\infty) = 0 \tag{A17}$$

$$\rho(0, x) = \rho(2\pi, x) \tag{A18}$$

plus an appropriate initial condition, such as $\rho(\theta, x, 0) = \delta(x - x_0)\,\delta(\theta - \theta_0)$.

Because the same time-scale constraints apply to this formulation, we must approximate the proton motion by the Markov process as before. Therefore, the equations describing the rotor and stator are

$$\frac{\partial \mathbf{p}}{\partial t} = \mathbf{L}_1 \cdot \mathbf{p} + \mathbf{L}_2 \cdot \mathbf{p} + \mathbf{K} \cdot \mathbf{p} \tag{A19}$$

where $\mathbf{p} = (p_E, p_T, p_B, p_F)^T$ is the state occupancy vector for the protons, and the diffusion operators $\mathbf{L}_1$ and $\mathbf{L}_2$ are given by

$$\mathbf{L}_1 = \left(D_r\left\{-\frac{\tau_{appl}}{k_BT}\frac{\partial}{\partial\theta} + \frac{\partial^2}{\partial\theta^2}\right\} + D_s\left\{\frac{1}{k_BT}\frac{\partial}{\partial x}(kx) + \frac{\partial^2}{\partial x^2}\right\}\right) \cdot \begin{pmatrix} 1 & 0 & 0 & 0 \\ 0 & 1 & 0 & 0 \\ 0 & 0 & 1 & 0 \\ 0 & 0 & 0 & 1 \end{pmatrix} \tag{A20}$$

$$\mathbf{L}_2 = \frac{1}{k_BT}\left(D_r\frac{\partial}{\partial\theta}\begin{pmatrix} \frac{\partial V_1}{\partial\theta} & 0 & 0 & 0 \\ 0 & \frac{\partial V_2}{\partial\theta} & 0 & 0 \\ 0 & 0 & \frac{\partial V_3}{\partial\theta} & 0 \\ 0 & 0 & 0 & 0 \end{pmatrix} + D_s\frac{\partial}{\partial x}\begin{pmatrix} \frac{\partial V_1}{\partial x} & 0 & 0 & 0 \\ 0 & \frac{\partial V_2}{\partial x} & 0 & 0 \\ 0 & 0 & \frac{\partial V_3}{\partial x} & 0 \\ 0 & 0 & 0 & 0 \end{pmatrix}\right) \tag{A21}$$

and $\mathbf{K}$ is the Markov matrix given in the text.

APPENDIX B: SMOOTH-RUNNING AND STEADY OCCUPANCY APPROXIMATIONS

In this section we examine the range of validity of the smooth-running approximation obtained by setting $\theta = \omega t$ and the steady-state occupancy approximation given in the text:

Smooth-running approximation:

$$\langle\tau_M\rangle \approx \frac{1}{T}\sum_{i=1}^{4}\int_0^{\tau} p_i(\omega t)\tau_M(\omega t)\mathrm{d}t \tag{B1}$$

Steady-state occupancy approximation:

$$\langle\tau_M\rangle \approx \sum_{i=1}^{4}\int_0^{2\pi} p_i(\theta)\tau_M(\theta)\mathrm{d}\theta \tag{B2}$$

Fig. 15 *a* shows the numerically calculated occupancy probabilities for a tethered cell with one functioning stator, along with the stationary state occupancy approximation. Even though the motor is turning very slowly compared to the proton hopping rates, the stationary approximation is poor. This is because with one stator the motor does not run smoothly (cf. Fig. 6 *a*). Fig. 15 *b* is the same as Fig. 15 *a*, but with eight stator elements working. For this case, the stationary state approximation is quite good, although there are still discernible differences, indicating that motor is not running completely smoothly, even with eight stators. Fig. 15 *c* shows the state occupancy probabilities for a free-swimming cell. In this case the stationary occupancy approximation fails because the motor speed is close to the hopping rate of the protons. The smooth-running approximation is good, although differences between the approximation and numerical results are still visible. Fig. 15 *d* shows the occupancy probabilities for a tethered cell with eight movable stators. The spring constant used in this figure was 4 pN/nm, and the x axis in these plots is the relative position between the rotor and stator. Note that these probabilities are similar to the stationary stator case with one active stator. This suggests that the motor is not operating smoothly, an observation confirmed by examining the first-passage statistics.

APPENDIX C: THE EFFECT OF STATOR ELASTICITY

Adding an elastic element to the stators is reminiscent of the "gumball" model of Berg and Khan (Berg and Khan, 1983; Meister et al., 1989). However, Berg's model is a "Brownian" ratchet, because its operating mechanism is based solely on rectifying the thermal motion of the stators. In contrast, the turbine model described here employs thermal energy to surmount potential barriers, but it also produces an electrostatic torque. In the Berg-Khan model, stator elements, being much smaller than the rotor, move on a time scale much faster than that of the rotor, and the flux of protons biases the stators' motion. The energy stored in the stator springs turns the rotor. The motivation for adding an elastic element was to improve the motors' performance under large viscous drag, where the slow diffusion of the rotor is the rate-limiting step.

In Fig. 16 we have plotted the average rotation rate as a function of the elastic constant, κ, for both high and low viscous drags. The solid line in each figure represents the stationary stator case. For small viscous drags, the stationary stator outperforms the motor with elastic elements, because the coupling between rotor and stator is tighter and the time for the rotor diffuse is not rate limiting. Surprisingly, at large viscous drags the elastic elements have little effect on motor performance. There are several factors that explain this. First, our model involves an electrostatic thrust that reduces the role of thermal fluctuations in driving the motor. Second, Meister et al. used a purely kinetic description to analyze their model (Meister et al., 1989). It is likely that this discretization increases the efficiency of energy transduction between the rotor and stator; however, further investigation into this question is needed before it can be answered definitively. Finally, allowing the much smaller stator to fluctuate does overcome the rate-limiting step involving rotor diffusion; however, the slowest time scale of the motor is now the time needed for the rotor to relax under the elastic force. This time scale is set by the ratio ζ_R/κ, the ratio of the friction coefficient of the rotor to the stator elasticity. This time scale may not differ appreciably from the diffusive time scale $\delta^2\zeta_R/(k_BT)$, where δ^2 is the distance over which the rotor must diffuse.

APPENDIX D: NUMERICAL METHODS

In this section we outline the numerical method we have employed to simulate the model's behavior. All numerical calculations were carried out using Matlab.

For stochastic simulation it is usual to choose a forward Euler discretization of Eqs. A.13 and A.14:

$$X(t + \Delta t) = X(t) + \Delta t\varepsilon\left(\frac{\partial}{\partial x}V(X - x, t) + \tau_{appl}\right) + \sqrt{2\varepsilon\Delta t}\Gamma_R \tag{D1}$$

$$x(t + \Delta t) = x(t) - \Delta t\left(x + \frac{\partial}{\partial x}V(X - x, t)\right) + \sqrt{2\Delta t}\Gamma_S \tag{D2}$$

where Γ_R and Γ_s are random numbers drawn from a Gaussian distribution with zero mean and unit variance (Doering, 1990). If the stator is in state i, the probability that a proton jump will occur during Δt is approximated by $(k_{i1} + k_{i2} + k_{i3} + k_{i4})\Delta t$. This probability is checked against a uniformly generated random number at each time step. If a transition does occur, another random number is generated and the probabilities $k_{ij}/(k_{i1} + k_{i2} + k_{i3} + k_{i4})$ are used to determine the state into which the proton jumps. Care must be taken to guarantee that the interval Δt is small enough that the probability of two transitions occurring during Δt is small. To ensure numerical accuracy, the rotor was spun at a slow fixed speed (i.e., $\mathrm{d}\theta/\mathrm{d}t = \omega$), and the numerically generated probability densities were compared against the steady-state distributions. The stators were spaced at a distance of $2\pi R/N + \Delta x$ around the rotor, where N is the number of stators and the

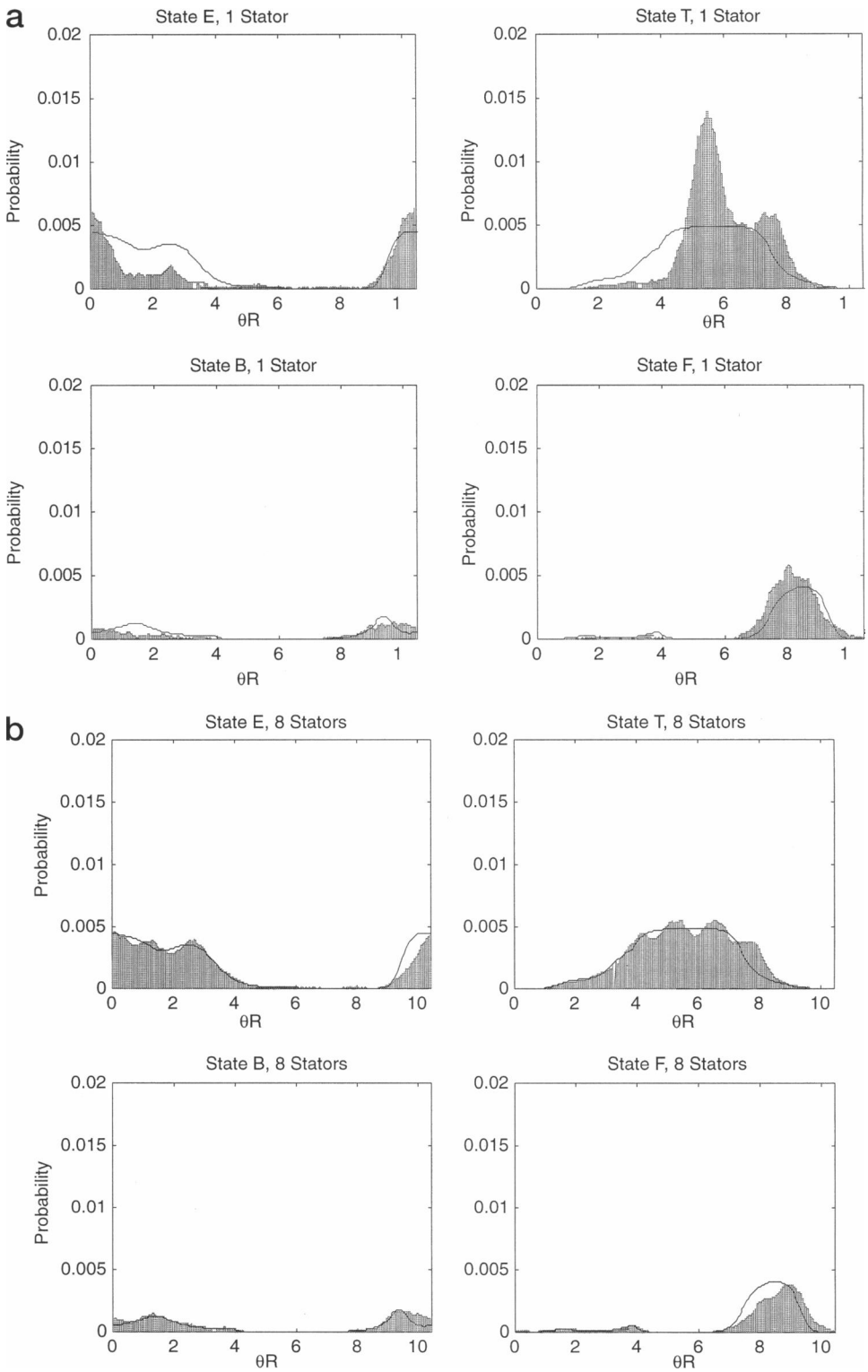

FIGURE 15 The stator state occupancies (E, T, B, F) as a function of the rotor's position. (*a*) A tethered cell with one functioning stator. The solid lines are the stationary occupancy approximations (Eq. B.2), and the shaded distributions are the numerically generated probabilities. (*b*) Same as in *a*, with eight functioning stators. (*c*) A free-swimming cell with eight functioning stators. For this case the solid lines were generated by the smooth-running approximation (Eq. B.1). (*d*) A tethered cell with eight movable stators.

distance Δx is a uniformly distributed random number between $\{-s/(2N), s/(2N)\}$, where s is the length of one repeating unit around the rotor. The random variable Δx helps to minimize the Vernier effect that arises when the stators are located symmetrically around the rotor. By iterating Eqs. D.1 and D.2 forward in time, the average angular velocity, $\langle v \rangle$, is calculated from $\langle v \rangle = X(t_f)/(2\pi R t_f)$, where $t_f = 0.5$ s. The first-passage statistics were

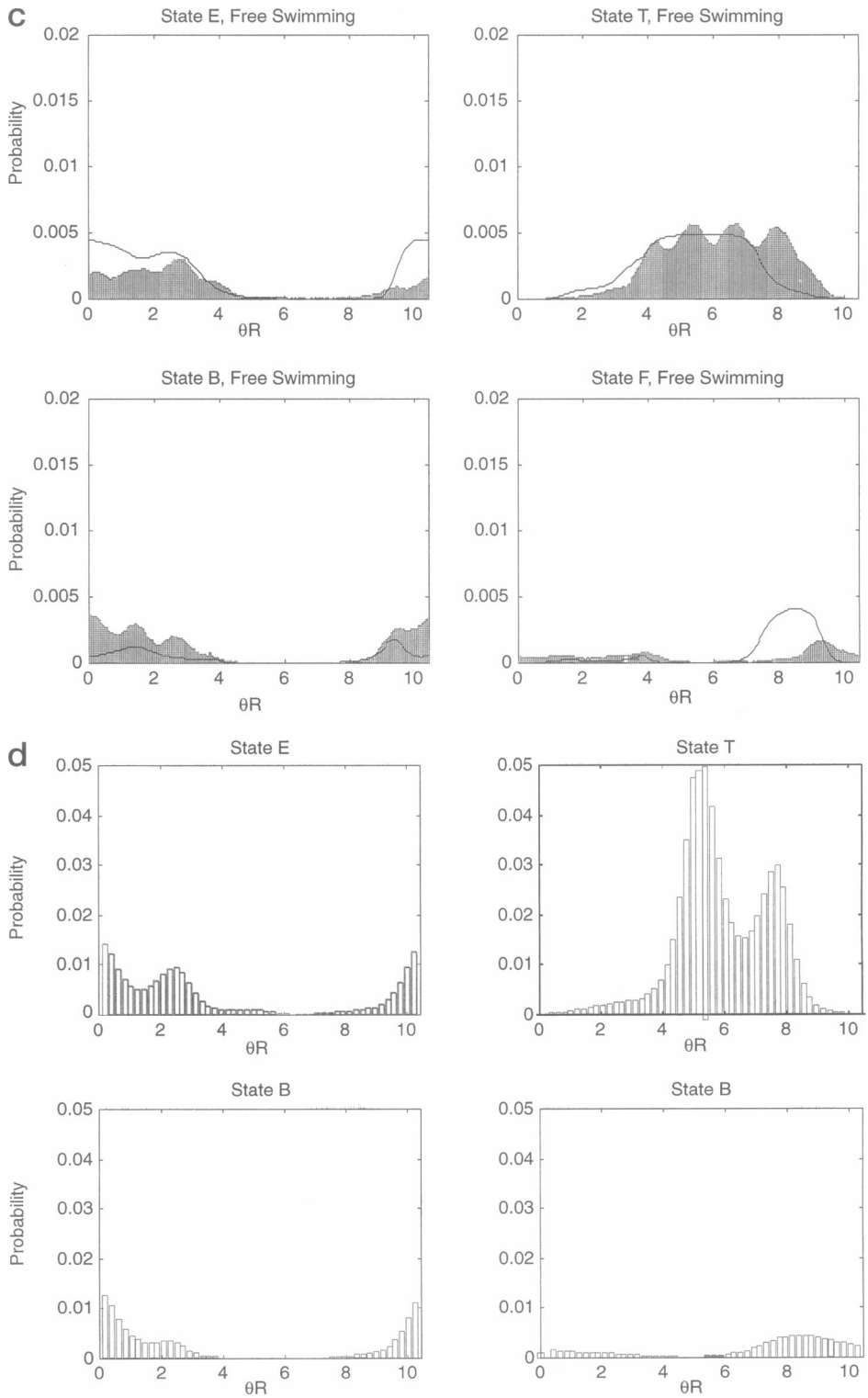

generated by averaging over 100 realizations of the time needed for the rotor to move through one revolution.

In the smooth-running approximation discussed in the text (under The Ion Turbine: Fixed Stator Model), $\theta = \omega t$ is substituted into Eq. D.1, making the right-hand side of these equations time dependent. Using the initial condition $p_i = 1/4$, the equations are then integrated forward in time, using the same Euler method discussed above. All of the results were obtained by integrating the difference equations over 10 periods of the cycle, to ensure that any transient behavior had decayed. All quantities were then calculated by averaging over one period according to Eq. B.1. In the stationary state approximation, the left-hand side of the equations in D.1 is set equal to zero, and the resulting set of linear equations is solved, subject to the constraint $p_1 + p_2 + p_3 + p_4 = 1$. Average values are then calculated according to Eq. B.2.

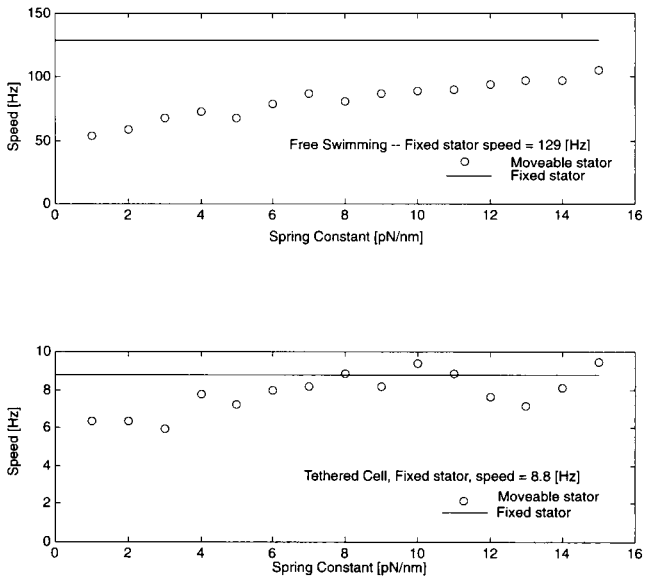

FIGURE 16 The effect of stator elasticity. The flexible stator does not improve the mechanical performance of the motor. The top panel shows that, for a free-swimming cell (low viscous load), the speed actually increases as the stator becomes more rigid. For a tethered cell (high viscous load), the speed is practically independent of the tether elasticity (*bottom panel*).

The authors thank Howard Berg, Richard Berry, Shahid Khan, Charles Peskin, and Linda Turner for their invaluable input. The reviewers' comments were unusually helpful in revising the manuscript in a major way.

TE was supported by Los Alamos National Laboratory. GO was supported by National Science Foundation grant DMS 9220719.

REFERENCES

Alberts, B., D. Bray, J. Lewis, M. Raff, K. Roberts, and J. Watson. 1994. *Molecular Biology of the Cell.* Garland, New York.

Anderson, R. 1975. Formation of the bacterial flagellar bundle. *In* Swimming and Flying in Nature. T. Wu, C. Brokaw, and C. Brennen, editors. Plenum, New York.

Berg, H. 1983. *Random Walks in Biology.* Princeton University Press, Princeton, N.J.

Berg, H. 1995. Torque generation by the flagella rotary motor. *Biophys. J.* 68:163s–166s.

Berg, H., and S. Khan. 1983. A model for the flagellar rotary motor. *In* Mobility and Recognition in Cell Biology. H. Sund and C. Veeger, editors. de Gruyter, Berlin. 485–497.

Berg, H., and L. Turner. 1993. Torque generated by the flagellar motor of *Escherichia coli. Biophys. J.* 65:2201–2216.

Berry, R. M. 1993. Torque and switching in the bacterial flagellar motor. An electrostatic model. *Biophys. J.* 64:961–973.

Berry, R., and H. Berg. 1996. Torque generated by the bacterial flagellar motor close to stall. *Biophys. J.* 71:3501–3510.

Childress, S. 1981. *Mechanics of Swimming and Flying.* Cambridge University Press, Cambridge.

Dean, G., R. Macnab, J. Stader, P. Matsumura, and C. Burks. 1984. Gene sequence and predicted amino acid sequence of the motA protein, a membrane-associated protein required for flagellar rotation in *Escherichia coli. J. Bacteriol.* 159:991–999.

Doering, C. 1990. Modeling complex systems: stochastic processes, stochastic differential equations, and Fokker-Planck equations. *In* 1990 Lectures in Complex Systems. L. Nadel and D. Stein, editors. Addison-Wesley, Redwood City, CA. 3–51.

Douady, S., and Y. Couder. 1992. Phyllotaxis as a physical self-organized growth process. 68:2098–2101.

Francis, N., G. Sosinsky, D. Thomas, and D. DeRosier. 1994. Isolation, characterization and structure of bacterial flagellar motors containing the switch complex. *J. Mol. Biol.* 235:1261–1270.

Hanggi, P., P. Talkner, and M. Borkovec. 1990. Reaction-rate theory: fifty years after Kramers. *Rev. Mod. Phys.* 62:254–341.

Huxley, A. F. 1957. Muscle structure and theories of contraction. *Prog. Biophys. Biophys. Chem.* 7:255–318.

Katayama, E., T. Shiraishi, K. Oosawa, N. Baba, and S. Aizawa. 1996. Geometry of the flagellar motor in the cytoplasmic membrane of *Salmonella typhimurium* as determined by stereo-photogrammetry of quick-freeze deep-etch replica images. *J. Mol. Biol.* 255:458–475.

Kleutsch, B., and P. Laüger. 1990. Coupling of proton flow and rotation in the bacterial flagellar motor: stochastic simulation of a microscopic model. *Eur. Biophys. J.* 18:175–191.

Laüger, P. 1977. Ion transport and rotation of bacterial flagella. *Nature.* 268:360–362.

Laüger, P. 1990. Microscopic models of the bacterial flagellar motor. *Comm. Theor. Biol.* 2:99–123.

Lloyd, S., and D. Blair. 1997. Charged residues of the rotor protein FliG essential for torque generation in the flagellar motor of *Escherichia coli. J. Mol. Biol.* 266:733–744.

Macnab, R. 1977. Bacterial flagella rotating in bundles: a study in helical geometry. *Proc. Natl. Acad. Sci. USA.* 74:221–225.

Macnab, R. 1996. Flagella and motility. *In Escherichia coli* and *Salmonella.* F. Neidhardt, editor. ASM Press, Washington, DC. 123–145.

Meister, M., and H. C. Berg. 1987. The stall torque of the bacterial flagellar motor. *Biophys. J.* 52:413–419.

Meister, M., S. R. Caplan, and H. C. Berg. 1989. Dynamics of a tightly coupled mechanism for flagellar rotation: bacterial motility, chemiosmotic coupling, protonmotive force. *Biophys. J.* 55:905–914.

Naber, H. 1996. Two alternative models for spontaneous flagellar motor switching in *Halobacterium salinarium. J. Theor. Biol.* 181:343–358.

Peskin, C., and G. Oster. 1995. Coordinated hydrolysis explains the mechanical behavior of kinesin. *Biophys. J.* 68:202s–210s.

Samuel, A., and H. Berg. 1995. Fluctuation analysis of rotational speed of the bacterial flagellar motor. *Proc. Natl. Acad. Sci. USA.* 92:3502–3506.

Samuel, A., and H. Berg. 1996. Torque generating units of the bacterial flagellar motor step independently. *Biophys. J.* 71:918–923.

Schnitzer, M. J., S. M. Block, H. C. Berg, and E. M. Purcell. 1990. Strategies for chemotaxis. *In* Biology of the Chemotactic Response. J. P. Armitage and J. M. Lackie, editors. Cambridge University Press, Cambridge. 15–34.

Schuster, S., and S. Khan. 1994. The bacterial flagellar motor. *Annu. Rev. Biophys. Biomol. Struct.* 23:509–539.

Sharp, L., J. Zhou, and D. F. Blair. 1995a. Features of MotA proton channel structure revealed by tryptophan mutagenesis. *Proc. Natl. Acad. Sci. USA.* 92:7946–7950.

Sharp, L. L., J. Zhou, and D. F. Blair. 1995b. Tryptophan-scanning mutagenesis of MotB, as integral membrane protein essential for flagellar rotation in *Escherichia coli. Biochemistry.* 34:9166–9171.

Svoboda, K., P. Mitra, and S. Block. 1994. Fluctuation analysis of motor protein movement and single enzyme kinetics. *Proc. Natl. Acad. Sci. USA.* 91:11782–11786.

Tang, H., T. Braun, and C. Blair. 1996. Motility protein complexes in the bacterial flagellar motor. *J. Mol. Biol.* 261:209–221.

Zhao, R., N. Pathak, H. Jaffe, T. Reese, and S. Khan. 1996. FliN is a major structural protein of the C-ring in the *Salmonella typhimurium* flagellar basal body. *J. Mol. Biol.* 261:195–208.